Summary of the First AIAA Stability and Control Prediction Workshop

Thomas Chyczewski, Andrew Lofthouse, Lie-Mine Gea, Aurelia Cartieri, Brett Hiller

Summary of the First AIAA Stability and Control Prediction Workshop

Tom Chyczewski[1]
Penn State Applied Research Lab, University Park, PA, 16804, USA

Andrew Lofthouse[2]
Air Force Life Cycle Management Center, Wright Patterson Air Force Base, OH, 45324, USA

Lie-Mine Gea[3]
The Boeing Company, Huntington Beach, CA, 92647, USA

Aurelia Cartieri[4]
ONERA, The French Aerospace Lab, 73500 Modane, France

Brett Hiller[5]
NASA Langley Research Center, Hampton, VA, 23681, USA

Results from the First AIAA Stability and Control Prediction Workshop are summarized in this paper. The workshop series was developed in support of three primary objectives: (1) to establish best practices for the prediction of stability and control derivatives using industry-standard Computational Fluid Dynamics (CFD) solvers, (2) to provide an impartial forum for evaluating the effectiveness of Reynolds-averaged-Navier-Stokes- and Detached-Eddy-Simulation-based modeling techniques, and (3) to identify areas in need of additional research and development. To address these objectives, the inaugural workshop focused on generating computational aerodynamic predictions for the ONERA version of the NASA/Boeing Common Research Model. The configuration includes the wing, body, horizontal tail, and a vertical tail designed by ONERA. While longitudinal wind tunnel test data for the model had been previously documented, unpublished lateral test data at small sideslip angles provided a unique opportunity for participants to generate blind computational predictions for wind tunnel data comparisons. Additional test cases included assessments of the Mach number effect on static lateral/directional stability and the impact of the wind tunnel sting on longitudinal stability. Participants were invited to generate solutions using two workshop-provided series of structured overset and unstructured grids, in addition to any participant custom grids of interest. Total and component-level breakdowns for the force and moment coefficients for each test case are presented, as well as sectional pressure distribution data on the wing and tail components, to assess the agreement between several different Reynolds-averaged Navier-Stokes CFD solvers.

[1] Associate Research Professor, Computational Mechanics Division, AIAA Senior Member.
[2] CFD Technical Expert, Flight Mechanics Branch, AIAA Associate Fellow.
[3] Associate Technical Fellow, The Boeing Company, AIAA Associate Fellow.
[4] Head of Experimental Group, Experimental and Development Unit, AIAA Member.
[5] Research Aerospace Engineer, Configuration Aerodynamics Branch, AIAA Member.

I. Nomenclature

α	=	angle of attack, degrees
AR	=	aspect ratio
β	=	sideslip angle, degrees
b	=	aircraft span, meters
C_D, CD	=	drag coefficient
C_L, CL	=	lift coefficient
CLL	=	rolling moment coefficient
CLM	=	pitching moment coefficient
CLN	=	yawing moment coefficient
C_p	=	pressure coefficient
CS	=	side force coefficient
M, Mach	=	Mach number
Re	=	Reynolds number
S_{ref}	=	reference surface area, meters squared
L_{ref}	=	reference length, meters
φ	=	potential field
u, v, w	=	x, y, z velocity components
x, y, z	=	Cartesian coordinates
y+	=	normalized first cell height
η	=	fraction of wing span, y/(b/2)

Acronyms

CFD	=	Computational Fluid Dynamics
CRM	=	Common Research Model
DPW	=	Drag Prediction Workshop
FUS	=	fuselage
HTP	=	horizontal tail plane
LRM	=	Large Reference Model
MAC	=	mean aerodynamic chord
PWNG	=	port wing
RANS	=	Reynolds-averaged Navier-Stokes
SA	=	Spalart-Allmaras turbulence model
SARC	=	Spalart-Allmaras turbulence model with the Rotation/Curvature correction
SCPW	=	Stability and Control Prediction Workshop
S&C	=	Stability and Control
SWNG	=	starboard wing
TAIL	=	horizontal and vertical tails
TE	=	trailing edge
TOT	=	total
VTP	=	vertical tail plane
WB	=	wing-body
WBH	=	wing-body with HTP
WBV	=	wing-body with VTP
WBVH	=	wing-body with VTP and HTP
WTT	=	wind tunnel test

Subscripts

m	=	model
s	=	support
∞	=	subscript for freestream state value

II. Introduction

PLATFORM issues associated with nonlinear aerodynamics revealed by flight test have plagued many aircraft development programs through the years[1-3]. These are oftentimes a result of wind tunnel dynamic testing limitations, poor scaling relationships between wind tunnel and flight Reynolds numbers, and, even today, the inability

of Reynolds-averaged Navier Stokes (RANS) based Computational Fluid Dynamics (CFD) to capture with sufficient fidelity vehicle forces and moments in flows dominated by these nonlinear aerodynamics. As a result, budget and schedule penalties, as well as possible envelope and performance penalties, are incurred. While the use of CFD to predict vehicle performance has matured significantly over the years, its role in Stability and Control (S&C) analysis has remained small. As pointed out in Ref. 1, there are a few reasons for this. Chief among them is that vehicle performance is generally confined to relatively benign regions of the envelope, while S&C analysis needs to consider off-design conditions, where complex aerodynamics that challenge RANS models are prevalent. This, combined with a lack of understanding of the limitations of the RANS approach by its early progenitors, led to a distrust of CFD by the S&C community.

An attempt at community consensus on the 2020 state of the art of S&C prediction was made in Ref. 4. In that work, existing capabilities of and limitations on methods to predict static and dynamic longitudinal and lateral directional stability, as well as control surface effectiveness for transport, fighter and flying wing configurations, were presented. It was agreed that CFD in its current form can and does support the S&C in a number of areas. Examples include downselecting candidate designs for wind tunnel testing, estimating Reynolds number scaling effects and wind tunnel sting increments, fine tuning configurations with respect to S&C and flight control laws, and supporting flight test by helping to distinguish the influence of static and dynamic derivatives in a maneuver, among others.

A path to expanding our capabilities was also put forth in Ref. 4 by defining low-hanging fruit that does not require significant turbulence modeling or computational power enhancements and high-hanging fruit that does. Among the low-hanging fruit are controlled examinations of 1) grid and geometry resolution effects on force and moment predictions and 2) unsteady simulations of various levels of fidelity (i.e., unsteady RANS to wall modeled large-eddy simulation), as well as the incorporation of crosswind, gust and ice accretion effects into S&C prediction. These are studies that can be pursued using today's capabilities and will likely have a meaningful impact on vehicle design. Higher-hanging fruit includes vehicle force and moment prediction when significant flow separation exists, some aspects of transonic flows (such as flow angle hysteresis and lift break angle of attack), approach/landing conditions, vortex lift, crossflow transition, time-variant dynamic derivatives and actuator hinge moment prediction, among others.

Many of the positions adopted in Ref. 4 were informed by a number of individual[5-9] and group[1,10-12] CFD studies (with and without companion wind tunnel tests). The group efforts consisted of collaborations between an invited set of investigators from different organizations that applied their own best practices to the same problem. Elements of these practices include discretization strategy (i.e., finite difference, finite volume or finite element), numerical scheme, grid generation and turbulence model. On the same timeframe, AIAA prediction workshops have been developed as another mode of collaboration. The universal objectives of these workshops, the inaugural of which was the First AIAA Computational Fluid Dynamics Drag Prediction Workshop (DPW1)[13], are to recruit a large number of participants through open solicitations to work on a set of common problems. A distinguishing aspect of most if not all of these workshops is the compulsory use of supplied grids (in addition to optionally using custom grids). As a result, a relatively large number of predictions are obtained in a controlled environment wherein grid generation, the best practice element traditionally accused of being a significant source of discrepancies between predictions, is eliminated as a variable. Further, the participants are required to provide results for a verification case to demonstrate that their codes are solving the governing equations as understood by the community. This is particularly important with respect to turbulence model implementations, which can require limiters or other tricks to obtain a stable and converging algorithm. These aspects of workshops are designed to tighten the spread between predictions to provide a clearer understanding of differences in performance between turbulence models for different problems.

The success of this approach is evidenced by the number of workshops that followed DPW1 thus far. These include five additional drag prediction workshops[14-18], three high-lift prediction workshops[19-21] and three sonic boom prediction workshops[22-26] among others. It was therefore natural to propose this approach as a way of advancing the state of the art in S&C prediction[4].

The objective of the first S&C prediction workshop is to establish a baseline with a relatively benign case to use as a foundation upon which to build. Towards this end, the geometry and conditions corresponding to an ONERA wind tunnel test of a variant of the Common Research Model (CRM)[27,28] were chosen for analysis. The CRM geometry has been used in several previous workshops (e.g., Refs 18 and 21) and has demonstrated its suitability for this type of environment. A compelling aspect of the ONERA test is that unpublished data at small sideslip angles were taken allowing for blind lateral directional cases. In addition, the geometry is identical to that used for previous workshops, including the aerodynamically loaded wings. Therefore, except for the vertical tail, which exists only for the ONERA model, grids developed from earlier workshops were able to be re-used here.

Detailed descriptions of the geometry and wind tunnel test are provided in the next two sections. Section V gives a description of the workshop test cases, while grid generation is described in Section VI. This includes the original

workshop provided structured and unstructured grids, as well as revised grids developed by three participants that were then distributed to all participants. Results and their discussion are presented in Section VII and conclusions are drawn in Section VIII.

III. Geometry

The CRM model developed by NASA and Boeing[28,29] serves as a reference for providing wind tunnel data aimed at the validation of codes dedicated to aircraft performance prediction. This model has been designed and built as part of the AIAA DPW series[13-18]. The model used in the current investigation is the ONERA Large Reference Model (LRM), which has the same geometry as the CRM.

A. Main dimensions

The ONERA LRM was sized to 220% of the NASA CRM, for a final scale of 1/16.835. This configuration consists of a contemporary, supercritical transonic wing (AR = 9.0) and a fuselage that are representative of a wide-body commercial transport aircraft. The vertical tail geometry was designed by the Civil Aircraft Unit of the Applied Aerodynamics Department in cooperation with the Wind Tunnel Division of ONERA[30].

The CRM is designed for a cruise Mach number of 0.85 and a corresponding lift coefficient of C_L=0.5. The ONERA model is defined by mean aerodynamic chord (MAC) L_{ref} = 0.4161 m, reference surface area S_{ref} = 1.3538 m², and a span b = 3.4905 m. The main dimensions of the model are given in Fig. 1.

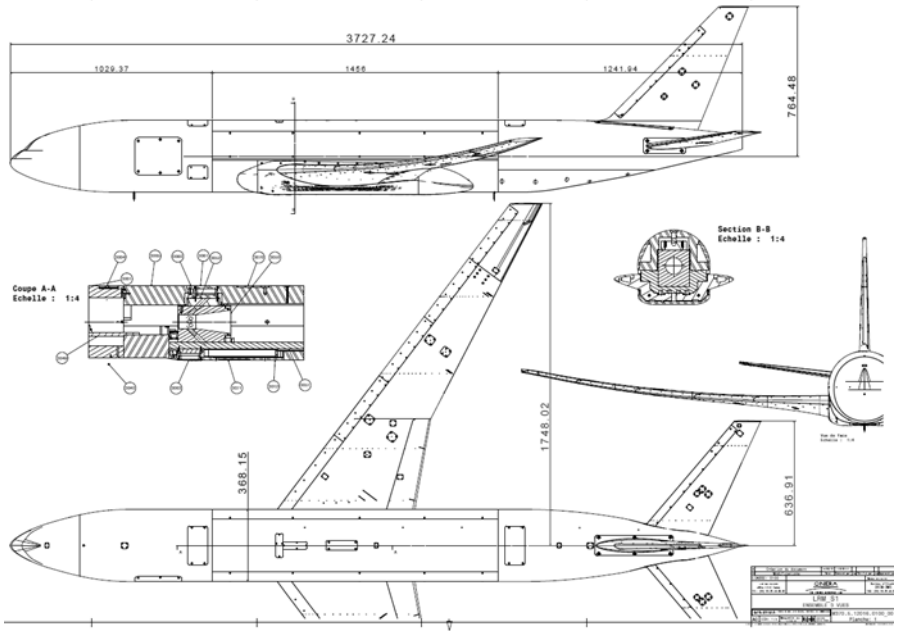

Figure 1. Main dimensions of the LRM model.

B. Wing shape

The ONERA LRM was designed so that it has the same deformation at the cruise point as the CRM tested in the National Transonic Facility (NTF).

The wing geometry used for the numerical computations of this study is the one corresponding to an experimental angle of attack of 2.75° and a lift coefficient of 0.5 proposed in the 6th AIAA Drag Prediction Workshop (DPW6) held in 2016, as shown in Fig. 2[27].

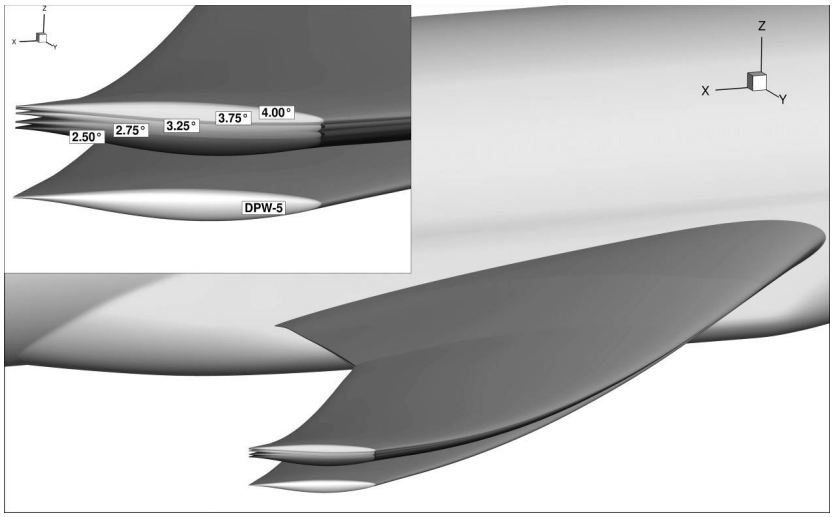

Figure 2. CRM wing shapes at different angles of attack.

IV. Wind Tunnel Test

A. Facility Description

ONERA's S1MA is a continuous atmospheric wind tunnel operating in the sub/transonic regime. It was put into service in 1952 and is equipped with two contra-rotating fans, driven by Pelton turbines, the power of which is 88 MW. The wind velocity can be varied from a few meters per second to approximately Mach 1 by varying the fan speed. The total length of the aerodynamic circuit is about 400 m (see Fig. 3). The test section dimensions are 14m in length and 8m in diameter. For a Mach number around 0.85, the unit Reynolds number is about 11 million per meter.

A peculiarity of the circuit is the absence of a heat exchanger. The temperature is controlled by letting outside fresh air enter the circuit. Hot air naturally exhausts around the edge of the contraction through an annular exit. An exhaust rate of about 10% of the total mass flow is required to maintain a temperature of about 50°C in the tunnel.

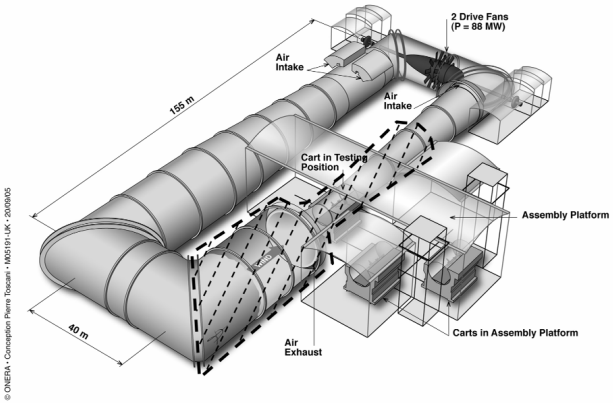

Figure 3. S1MA air circuit.

B. History

At the end of 2014, the first test campaign involving the LRM took place in S1MA. The main purpose of this test was to acquire a large reference database on this model. Measurements such as force and moment quantification (balance), dynamic and static skin pressure probing, and surface flow visualization have been performed for large ranges of Mach numbers (0.30 to 0.95) and lift levels. Four configurations of the model have been assessed in the

wind tunnel: the Wing-Body only (WB), the WB with Horizontal Tail Plane (WBH), the WB with Vertical Tail Plane (WBV), and finally the WB with both Vertical Tail Plane (VTP) and Horizontal Tail Plane (HTP) (WBVH). Then, several wind tunnels campaigns have been performed, including sideslip tests in 2016. The model is mounted in the wind tunnel using a Z sting (or swept blade mount) setup as shown in Fig. 4.

C. Test Conditions and Measurements

The tests were carried out in a Mach number range going from *Mach* = 0.30 up to *Mach* = 0.95. The Reynolds number based on MAC was 5 million. The incidence range was from -3.0° to +10.0°. Some sideslip polars were performed (+/-1°) in a Mach number range going from *Mach* = 0.7 up to *Mach* = 0.9 and an incidence range from -3.0° to +4.5°

The incidence of the model was measured by means of three goniometers connected to the weighed balance adapter. It was corrected for wall and sting effects (see below) and for the wind tunnel up-wash that was determined during the campaign.

The loads of the model were measured with a six-component balance. All pressure measurements were made using Electronically Scanned Pressure (ESP) modules installed inside the forward portion of the fuselage. Pressure distributions are measured on both the port and starboard wings using 270 pressure orifices located in 9 spanwise stations: 5 on the starboard wing (η = 0.131, 0.283, 0.502, 0.727 and 0.950) and 4 on the port wing (η = 0.201, 0.397, 0.727 and 0.846) . There was also one section on the VTP, and three sections on the HTP (η = 0.2, 0.5 and 0.8). The fuselage was also equipped as shown in Fig. 5.

Figure 4. The LRM model in S1MA wind tunnel.

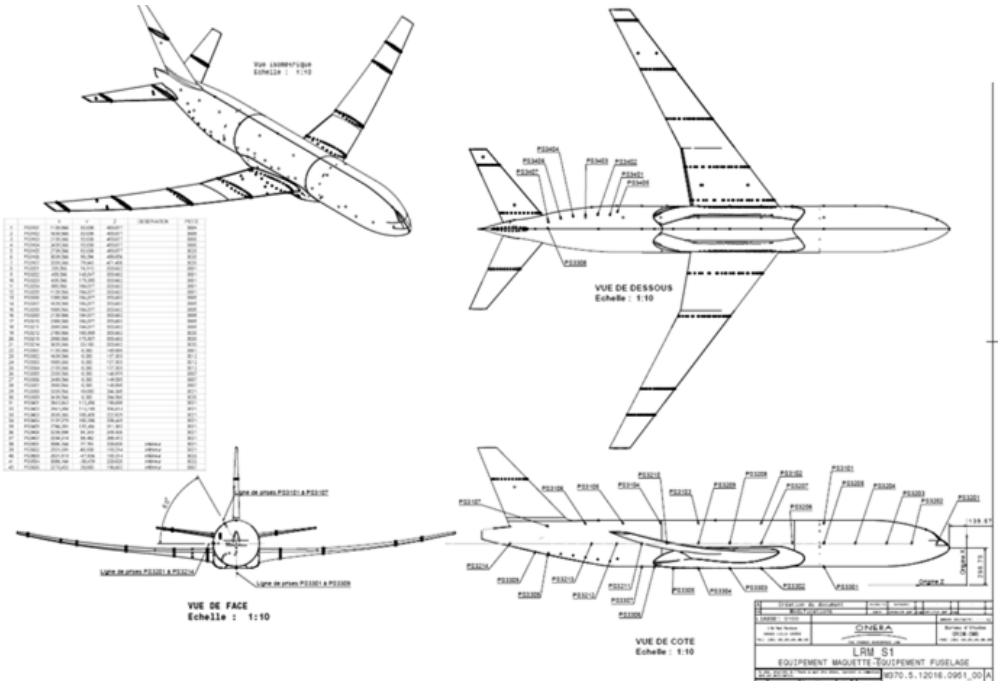

Figure 5. Pressure measurement locations.

The wing deformation measurements were performed in real time with two high resolution cameras located in the ceiling of the test section[31] behind a window. The bending and twist deformations of the starboard wing were derived from the comparison of the 3D target positions between wind-on and wind-off conditions. The deformation measurements obtained at $Mach = 0.85$ and $C_L = 0.5$ were in good agreement with the results obtained in the NTF and European Transonic Windtunnel (ETW).

The transition of the boundary layer on the different parts of the model was forced by means of CADCUT strips. Trips measuring 1.3 mm in diameter and spaced 2.4 mm apart were used for the entire test. The trip dots were installed at 10% chord on the wings, the HTP, and the VTP. The trip dots were 0.142 mm high on the wing and 0.127 mm high on the tails. On the fuselage, the trips were applied at 60 mm from the nose and measured 0.152 mm high. Some acenaphthene visualizations were performed at the beginning of the test campaign in order to check the effectiveness of the boundary layer tripping. Finally, some colored oil flow visualizations were also performed.

D. Data acquisition and reduction

All model internal sensors were continuously recorded at a sampling rate of 1 Hz, with a low-pass filter of 0.2 Hz. The α sweep speed was about 0.2 °/s. The aerodynamic coefficients of the model obtained during α sweeps were interpolated in Mach number, using 3 points and 2nd degree polynomial equations.

E. Correction Methods

The aerodynamic interferences are taken into account thanks to a correction process composed of several contributions:

1) The empty test section correction, which is a Mach number correction that results from a test section tunnel calibration;
2) The buoyancy correction: it is the effect of the empty wind tunnel Mach number gradient on drag (which is proportional to the product of the gradient and the effective volume of the body);
3) The wall effect correction: these corrections rely on potential flow theory[32]. Under the assumption that the flow in the tunnel is irrotational outside the boundary layers and wakes, it can be described by a velocity potential $U_0 x + \varphi$. Assuming now that the velocity perturbations $\partial_x\varphi$, $\partial_y\varphi$ and $\partial_z\varphi$ are small with regard to U_∞, one comes to the well-known linearized potential equation:

$$(1 - Ma_\infty^2)\partial_x^2\varphi + \partial_y^2\varphi + \partial_z^2\varphi = 0 \quad (1)$$

with boundary conditions at solid walls linearized as well.

Unfortunately, this last assumption is less and less valid as the upstream Mach number M_∞ approaches 1 and as typical transonic phenomena occur on the model, with large fluid accelerations up to the supersonic regime. This equation and the corresponding boundary conditions can be solved through a distribution of singularities on the model and support. The intensity of each singularity is based on the cross section areas, lift and drag.

Once the proper singularities have been set up, the linearity of Eq. (1) allows the potential φ to be broken down into a field φm generated by the model and a field φs generated by the support. Hence $\nabla\varphi_s = (u_s, v_s, w_s)$ is the field of velocity distortion generated by the support. Once the velocity field $\nabla\varphi_s$ is known, one can easily determine a field of Mach number distortion:

$$\delta M = M_\infty \left(1 + \frac{\gamma-1}{2} M_\infty^2\right) \frac{u_s}{U_\infty} \quad (2)$$

and a field of angle of attack distortion (upwash):

$$\delta\alpha = \frac{w_s}{U_\infty} \quad (3)$$

These fields are then averaged in space over areas of aerodynamic significance.

The Mach number correction ΔM is taken as the value of δM at ¼ of the MAC. The α correction is computed from a slightly more elaborate process: it is chord-averaged along the wing span and taken at ¾ of local chord. This correction enabling the lift correction to be zero (theory of Pistolesi[33]).

Second order corrections on drag (buoyancy correction due to velocity distortion) and pitching moment (mainly due to the HTP lift gradient to α) are then calculated.

4) The sting corrections: these corrections are calculated with RANS computations[34,35]. First-order corrections are determined using a pairing process. With and without support simulations are considered as paired when the flow fields around the wing are similar. The criterion of similarity is the Root Mean Square (RMS) of pressure coefficient distortion on the wing. The corrections to forces and moments are deduced from the differences between the integrated forces over the model with and without support. For the purpose of this study, those sting corrections were not taken into account as the sting geometry was modelled by CFD.
5) The sting cavity pressure correction: this correction results from the presence of a pressure coefficient (not zero) inside the rear fuselage, which is "open" to enable sting entry. It consists of replacing, on the cavity surface, the mean measured cavity pressure by the reference pressure.

V. Test Case Descriptions

The first case was included in the workshop to verify that the codes used by the participants are solving the governing equations as understood by the community. As mentioned earlier, this is particularly useful to confirm that their turbulence model implementation is sound. The case is the 2D NACA 0012 airfoil and was taken from the NASA Langley Research Center Turbulence Modeling Resource website[36]. Participant results are not presented in this paper.

For the remaining cases, the specified Reynolds number is based on the MAC (Re) and freestream airspeed, the forces and moments are in the stability axis system, the yawing and rolling moments are normalized by the full span, and the pitching moment is normalized by the wing MAC. For cases that include the wind tunnel sting, the forces and moments are not integrated over the sting (only LRM contributions are included). The total LRM forces and moments are determined by summing the contributions from the port wing (PWNG), starboard wing (SWNG), fuselage (FUS) and tail (TAIL) reported by the participants.

Case 2 is a grid convergence study for the LRM and wind tunnel sting geometry. The flow conditions are: β = 1° nose left, Mach 0.83, Re_{MAC} = 4.56 million and CL = 0.5 (the angle of attack is iterated upon until the target lift is achieved). Solutions obtained using the coarse, medium and fine grids are required as a minimum. This is a common workshop case and is intended to assess our ability to reach grid converged forces and moments and to see how they compare between participants.

The subject for Case 3 is the Mach effect on static lateral/directional stability. The sideslip angle β = 1° nose left and a target CL=0.5 was specified. Results obtained at the time the workshop was held were for Mach numbers 0.70, 0.83, 0.87 and 0.90 (with corresponding Reynolds numbers based on MAC were 4.26, 4.56, 4.61 and 4.68 million,

respectively). However, it came to light, after many of the participants had already performed the runs, that these Mach numbers are corrected to account for the wind tunnel sting. Following the workshop, the participants re-ran these cases with the uncorrected Mach numbers plus an additional Mach number to improve resolution of a force and moment break. The final sweep was Mach 0.7019, 0.8325, 0.8530, 0.8749 and 0.9050, with corresponding Reynolds numbers based on MAC of 4.24, 4.56, 4.60, 4.62 and 4.7 million (note that the wind tunnel data are for Mach 0.8740, not 0.8749). Given the symmetric geometry, the side force, rolling moment and yawing moment at $\beta = 1°$ are also the derivatives with respect to β (per degree) at $\beta = 0°$ calculated using a central difference scheme. Participants were only required to submit results using the medium grids.

While Cases 2 and 3 are focused on lateral directional stability, Case 4 looks at the impact of the wind tunnel sting on longitudinal stability. The LRM was run both with and without the sting at $\beta = 0°$ and Mach 0.83 (Re_{MAC} = 4.56 million). For the workshop, participants were asked to run at two lift coefficients, 0.48 and 0.52 so that dCLM /dCL at CL=0.5 could be calculated and also at two angles of attack, 2.9° and 3.0° so that dCLM /dα at 2.95° could be calculated. However, the comparisons are very similar (α for CL=0.5 is around 3°) so only the dCLM /dCL results are presented in this paper for brevity. Participants were only required to submit results using the medium grids. The goal for this case was to see how well the results from the participants agreed since there is no wind tunnel data available.

Case 5 was optional and was intended to give the participants an opportunity to utilize their own best practices to determine the lateral directional stability derivatives at $\beta = 0°$ instead of employing the central difference scheme used for Case 2. There were not enough results submitted for this case to get any meaningful statistics, so no results for this case are presented here.

Finally, Case 6 is a wider β sweep (1°, 3° and 5°) using the same conditions as Case 2 except only results from the medium grid were solicited. Wind tunnel data are only available for β = -1°, 0° and +1° so this is another case where comparisons are made only between participant results. This was an optional case.

VI. Grid Generation

A. Structured Overset

- Original Workshop Grids

The overset grid system for the workshop was assembled by the Air Force Research Laboratory (AFRL). All component grids except the vertical tail and sting grids were taken from DPW6 wing-body (WB) and DPW4 horizontal tail (H). DPW6 achieves a 1.5 grid point scaling factor by utilizing a unique scaling factor for each grid direction. Details of grid generation for DPW6 can been found in reference[37]. Some of the important parameters used in DPW6 are listed in Table 1. Five grid levels (Tiny, Coarse, Medium, Fine, Extra Fine) were chosen for the SCPW1 study. The surface grids for the five grid systems are shown in Fig. 6.

The newly generated vertical tail and sting grids for this workshop were done using NASA's Chimera Grid Tool (CGT) 2.1 package[38] with one exception done in Pointwise™ [39]. These new grids closely follow the guidelines in DPW6, however, to maintain two levels of multigrid and due to some geometric complexity, the exact 1.5x growth factor is not maintained in some grids.

Table 1. Workshop provided structured overset grid parameters.

Level	Viscous spacing (in)	~y+	# of const. cells at wall	Max. stretching	Grid size (vertices)
Tiny	0.001478	1.02	4	1.235	26,814,781
Coarse	0.001182	0.80	5	1.186	46,741,528
Medium	0.0009853	0.67	5	1.149	83,513,624
Fine	0.0008446	0.58	6	1.128	146,048,258
Extra Fine	0.0006569	0.50	7	1.112	274,548,224

The Wing-Body-Horizontal Tail (WBH) grids taken from DPW6 and DPW4 (full-scale, half body) are scaled down to the model scale using a scale factor of 0.0594 (1/16.835). To address the side-slip effect, the full body configuration is required. The half model body (or semispan) grids are mirrored and concatenated on a symmetry plane to make a single grid. No adjustment was made to smooth the grid lines across the symmetry plane. Both the nose cap and tail cap grids are modified for the full body configuration. Wing and horizontal tail grids are mirrored to

form the full body grid system. In total, there are three fuselage grids (body, nose cap and tail cap), three grids for each wing (wing, wing-body collar and wing tip cap) and six grids for each horizontal tail (horizontal tail, body-horizontal tail collar, horizontal tail cap, and three grids to resolve the horizontal Trailing Edge TE).

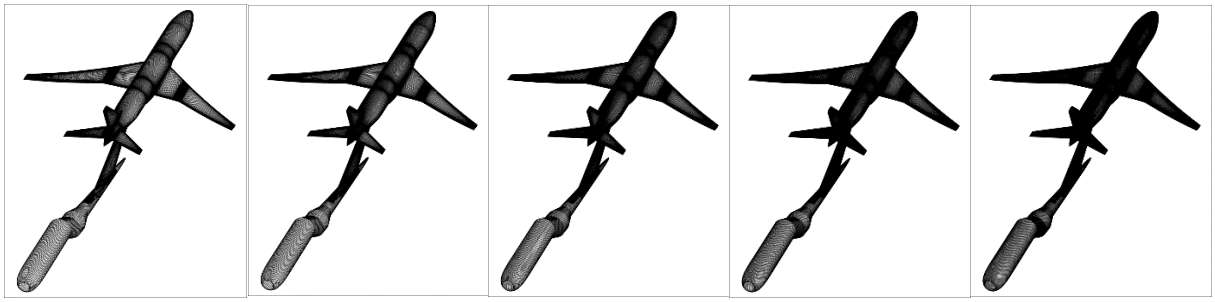

Figure 6. Structured overset surface grids (from left to right: Tiny, Coarse, Medium, Fine and Extra Fine)

The box grids taken from DPW6 also needed to be scaled and mirrored to reflect the full body model scale configuration. In particular, the inner box is modified to extend the fine grid resolution downstream and upward to cover the vertical tail and support sting.

For the vertical tail, the grids are generated from scratch using the CAD geometry, using a standard three-grid topology. An O-type grid is used to wrap around the airfoil and the TE, an H-type grid is used for the tip and another O-type grid is generated for the body-vertical tail collar. The detailed grid spacing parameters for different level of vertical tail grids are shown in Table 2.

Table 2. Vertical tail grid spacing parameters.

	TINY	COARSE	MEDIUM	FINE	XFINE
Spacing Scale Factor	1.0	0.875	0.763	0.667	0.582
ΔS_{LE} / ΔS_{TE} / ΔS_{MAX}	0.2 / 0.1 / 2.0	0.175 / 0.0875 / 1.751	0.153 / 0.0763 / 1.526	0.133 / 0.0667 / 1.333	0.116 / 0.0582 / 1.165
ΔS_{TIP} / ΔS_{ROOT} / ΔS_{MAX}	0.2 / 0.1 / 1.5	0.175 / 0.0875 1.3131	0.153 / 0.0763 / 1.145	0.133 / 0.0667 / 1.000	0.116 / 0.0582 / 0.8736
ΔS_{wall}	0.000133	0.000114	0.000101	0.0000887	0.0000775
N_{wall}^{const}	2	2	3	4	5
N_{TE}	5	9	13	17	21

Spacing scaled per guidelines from DPW6 →

- **Grow Next-Finer Grid in Family by ~ 1.5X in Size**
  - Scale Dimensions in All Three Computational Directions by ~ 1.15X
  - Grid Spacings Reduce by 0.87=(1/1.15) per Mesh Level
    - 0.1% in Tiny → [T,C,M,F,X,U] = [0.100, 0.087, 0.076, 0.066, 0.057, 0.050]%

The ONERA wind tunnel model support sting geometry is also included in the workshop simulations. The support sting consists of an axisymmetric sting body and a vertical blade that connects the sting and LRM fuselage. Four grids are generated for the axisymmetric sting, two O-type grids around the perimeter of the sting and two cap grids for front and rear ends. A total of five grids are needed for the swept blade. Two O-type grids for the main part of the blade and the LRM-blade collar. Due to the shallow angle in the blade and sting junction region, the typical collar grid is divided to a three-grid topology with a C-type grid for the main collar plus two H-type grids to cover the blade TE/body junction area. The medium surface grids for the vertical tail and sting support are shown in Fig. 7.

Finally, a detailed breakdown of grid numbers and points for wing/body (L+R), horizontal tail (L+R), vertical tail, sting and background boxes are listed in Table 3.

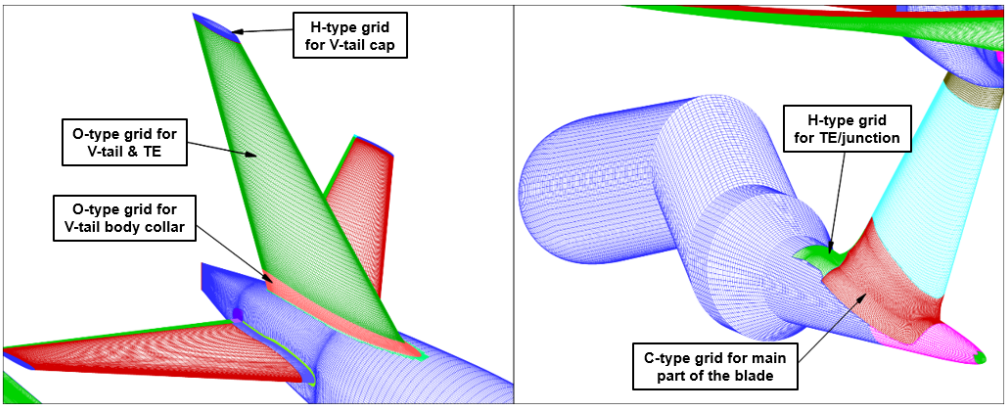

Figure 7. The medium surface grids for the vertical tail and sting support.

- Revisions Based on Workshop Findings

Issues with the structured overset vertical tail grids came to light during the workshop when results obtained with them were observed to be in poor agreement with the unstructured grid results and to the wind tunnel test data. For instance, the contribution of the vertical tail to the side force (see Figs. 21 and 22 in section VII) and yawing moment (see Figs. 27 and 28 in section VII) are considerably scattered and uniformly offset from the unstructured grid results (compared to contributions from the other LRM components) as the grid is refined. The predicted total side-force and yawing-moment variation with Mach number also agreed less favorably with the wind tunnel test data.

A subsequent inspection of the grids uncovered a couple of issues that are illustrated in Fig. 8 for the medium grid. One is the very large spacing near the leading edge. As indicated in Table 2, it was set to be about 10% of the maximum spacing along the chord. For the total number of grid points in this direction, it leads to leading-edge spacing that will not sufficiently capture the stagnation region. The other issue is surface faceting, wherein the surface is represented as a series of flat panels rather than a smooth surface. This can be seen in Fig. 8 as abrupt changes in the surface shading, which is more drastic in the chordwise direction.

Table 3. Structured overset grid parameters.

From DPW6 Grid Generation Guidelines →

- **Grow Next-Finer Grid in Family by ~ 1.5X in Size**
  - Scale Dimensions in All Three Computational Directions by ~ 1.15X
  - Grid Spacings Reduce by 0.87=(1/1.15) per Mesh Level
    - 0.1% in Tiny → [T,C,M,F,X,U] = [0.100, 0.087, 0.076, 0.066, 0.057, 0.050]%

No. of Grids	9 (3B + 3LW + 3RW)		12 (6L + 6R)		3		9		3		36	
Name	No. GP (M)	Growth Factor	No. GP (M)	Growth Factor	No. GP (M)	Growth Factor	No. GP (M)	Growth Factor	No. GP (M)	Growth Factor	No. GP (M)	Growth Factor
	Wing/body (L + R)		Horz. Tail (L + R)		Vert. Tail		Sting		Background		Total	
TINY (T)	9.1	-	4.0	-	1.1	-	2.2	-	10.3	-	26.8	-
COARSE (C)	17.6	1.9	4.0	1.0	1.8	1.6	3.5	1.6	19.8	1.9	46.7	1.7
MEDIUM (M)	30.2	1.7	9.3	2.3	2.9	1.6	5.1	1.5	34.9	1.8	82.4	1.8
FINE (F)	47.8	1.6	31.1	3.3	4.5	1.6	7.8	1.5	54.8	1.6	146.0	1.8
EXTRA-FINE (XF)	71.1	1.5	104.1	3.3	6.5	1.4	10.9	1.4	81.9	1.5	274.5	1.9

Reused from DPW6 w/ mods done for current workshop

Reused from DPW4 w/ mods done for current workshop

Created for current workshop

Reused from DPW6 w/ mods done for current workshop

A participant from Northrop Grumman assumed the responsibility of generating new mesh families for the vertical tail. The leading-edge resolution and surface smoothness issues were resolved. In addition, wall spacing uniformity, grid overlap quality and point clustering smoothness were improved. A side-by-side comparison of the two surface grids is shown in Fig. 9. The new grids were distributed to the workshop participants who were asked to use them to get updated results for the Mach sweep case (Case 3). All Case 3 results presented here were obtained using these grids. It was decided that it was not practical to do Case 2 over again given the computational resources it requires. The vertical tail is not a significant factor in Case 4 since there is no sideslip.

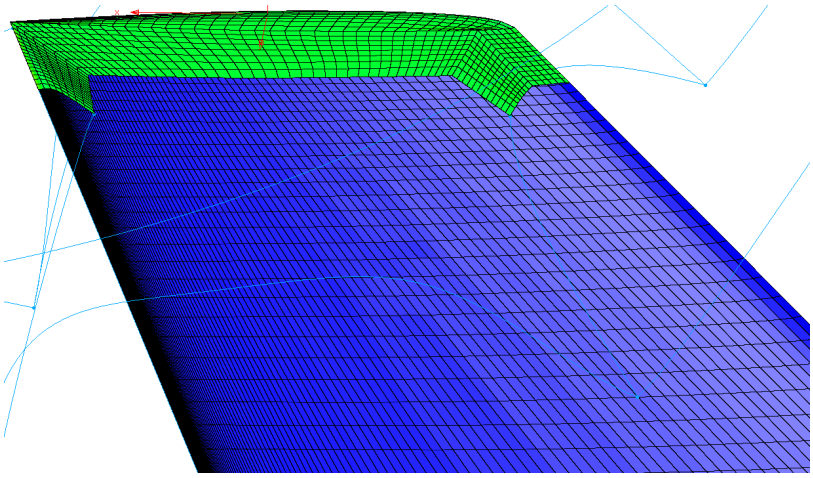

Figure 8. Side view of the original medium vertical tail surface grid.

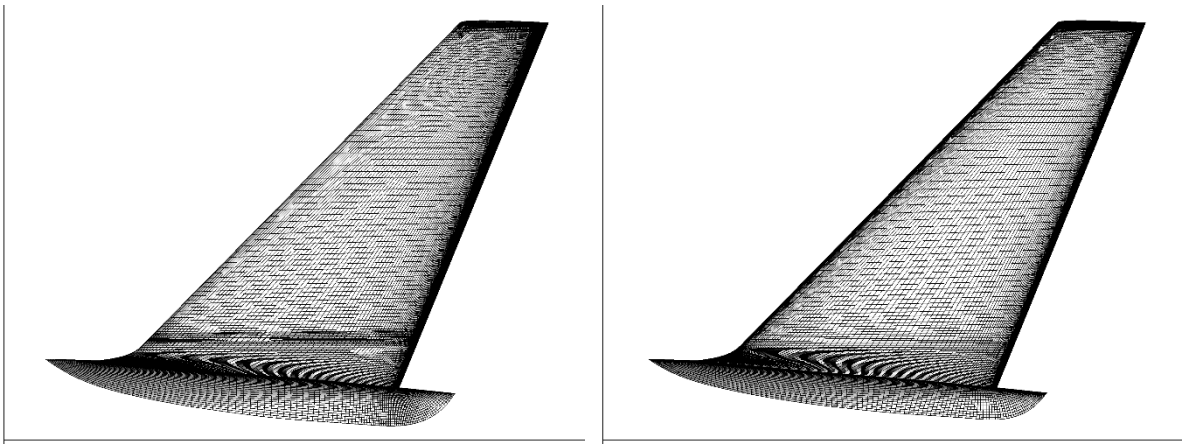

Figure 9. Comparison of the original (left) to the revised (right) medium vertical tail surface grids.

B. Unstructured

Three different sets of unstructured meshes were used for the workshop. One set was generated using Pointwise™ [39] by the software developers and provided by the workshop committee to participants. Two other sets of unstructured meshes were created by individual participants to supplement the committee-provided meshes.

- Common Unstructured Mesh Family

The common mesh family, provided by the committee, included five levels of hexahedra and tetrahedral meshes. Mesh sizes ranged from 20 to 74 million cells for coarsest to finest. The following description outlines the general process used to create the meshes.

The geometry was reviewed to see if any modifications or adjustments were needed to prepare it for mesh generation. Once a clean watertight geometry was obtained, a few initial "tiny" level meshes were created and iterated with committee members to determine refinement locations for the meshes, as well as a good starting resolution to use. With the tiny mesh established, it was systematically refined by a factor of 1.15 to create the next mesh refinement level. Subsequent levels were created in the same manner. Once the medium level was finished, some final tweaks were required, and the final meshes were created by systematically coarsening and refining the medium mesh.

Quad-dominant surface meshes were generated in a largely automatic fashion on the geometry. After they were generated, additional spacing controls were applied to cell edge lengths on the surface mesh regions with sharp feature

edges to better resolve these areas (such as the aft fuselage closure and the sharp trailing edge on the sting). Spacing controls were also applied to regions of high curvature using a relatively new feature in Pointwise™ [39] that allows specification of a desired bending angle, rather than an initial height, for growing anisotropic layers in the surface mesh. This method produces a variation in cell heights along curved surfaces (such as wing leading edge) based on the curvature of the underlying geometry. This effect can be seen on the close-up of the wingtip TE where the layers fan out due to the difference in curvature and in the close-up of the wingtip LE, where the layers are more aligned due to more consistent curvature. A bending angle of 10 degrees was applied along the leading edge of the wings and 15 degrees along the leading edges of the tail fins and sting. The mesh refinement factor was also applied to these angles to maintain consistency throughout the mesh family. The resulting angle values are shown in Table 4.

Once the surface meshes were set up, the volume mesh was generated by growing anisotropic layers of prisms and hexahedra off the surface mesh, which then transitioned into isotropic tetrahedral for the remainder of the volume. The initial cell height from the wall, as well as the geometric growth rate, used is in the table. Anisotropic mesh layers were stopped if they reached a prescribed isotropic height, collided with an encroaching mesh front or boundary, or if cell-quality criteria were exceeded.

Visualizations of the Tiny level of the common unstructured mesh family, including the details of the structured mesh at the knife-edge fuselage trailing edge, and the wing tip (from above and behind) are shown in Fig. 10. Views of the other mesh refinement levels (Coarse, Medium, Fine and ExtraFine) are shown in Fig. 11. In particular, note the refined trailing edges of the wings (similar spacing is used for the tails and fuselage).

Table 4. Grid characteristics of the Common Mesh Family.

Mesh	Bending Angle (deg)		Wall Spacing	Growth Rate	Points Across TE	Viscous Layers	Total Cells (M)	Total Points (M)
	Tail Wingtip Sting	Wing						
Tiny	15	10	1.3300E-04	1.200	17	56	20.4	14.6
Coarse	13.04	8.69	1.1565E-04	1.172	19	64	27.8	20.3
Medium	11.34	7.56	1.0062E-04	1.148	23	74	38.1	28.3
Fine	9.86	6.57	8.7480E-05	1.127	27	85	52.0	39.5
Extra-Fine	8.57	5.71	7.6050E-05	1.110	31	97	74.2	53.9

- USAF AFLCMC grids

A series of mesh families were generated by the US Air Force Life Cycle Management Center (AFLCMC) to conduct an in-depth study of the effect of cell type on the CFD analysis and final stability and control parameters. These meshes were also generated using a Pointwise ™ [39] parameterized script. The Level 0 (Tiny) mesh sizing closely followed the sizing of the initial committee-provided common mesh. Higher levels were obtained by changing the script parameters by a factor 1.15 (including the boundary decay, the growth rate and the maximum viscous layers). Several mesh families were generated as follows.

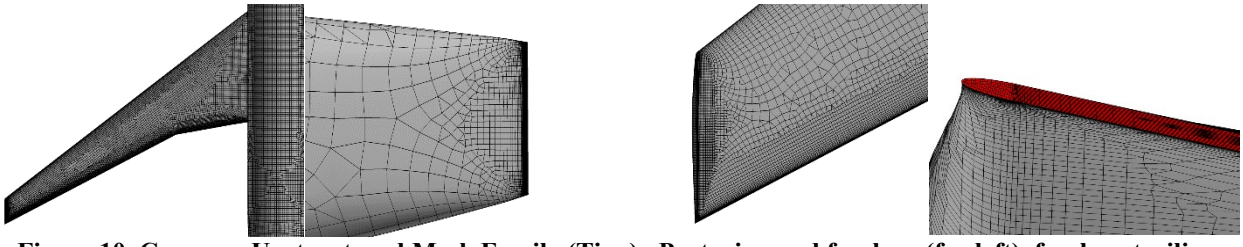

Figure 10. Common Unstructured Mesh Family (Tiny). Port wing and fuselage (far left), fuselage trailing edge (left), upper view of wing tip (right), and aft view of wing tip (far right).

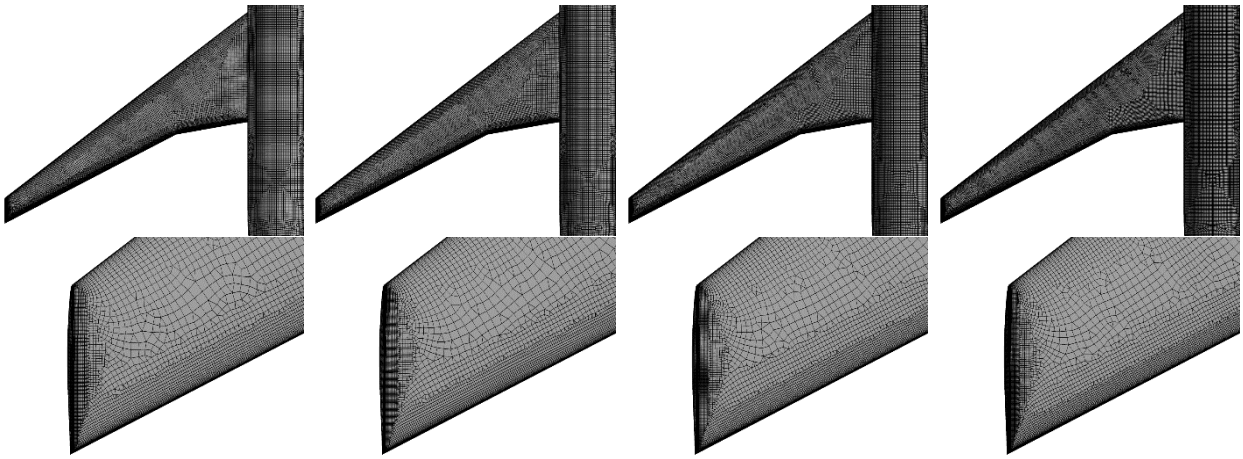

Figure 11. Common Unstructured Mesh Family. Port wing and fuselage (top row); wing tip detail (bottom row). Coarse (far left), Medium (left), Fine (right), ExtraFine (far right).

The L1 family was an attempt to mimic the committee-provided mesh. It used a quad-dominant surface meshing strategy with a structured surface mesh to refine the sharp fuselage trailing edge. The L3 family was similar to L1, but did not use the structured surface mesh along the fuselage trailing edge. The L4 family was tri-dominant (all surface elements were triangles instead of quadrilaterals). The L5 family was a hybrid of quad- and tri-dominant surface elements; quads were used in the anisotropic regions while triangles were used elsewhere. The L6 family was quad-dominant but with more coarsened trailing edges than the common mesh family. Finally, the L7 family was also quad-dominant but used more refined trailing edges than L6 (but not as much as the common mesh family). The characteristics of this grid family are provided in Table 5. Note that with the same mesh spacing constraints, tri-dominant meshes contain more cells than quad-dominant meshes. Mesh characteristics for the AFLCMC mesh families, such as initial wall spacing, growth rate and points across the trailing edges, are shown in Table 6. These mesh characteristics are very similar to those for the common unstructured mesh family shown in Table 4, with three exceptions. First, there are additional mesh levels (note that Level 1 corresponds to the Tiny mesh, etc). Second, the number of points across the trailing edge varies according to the mesh family: for families L1-L5, the number of points is similar to the common unstructured mesh families, but mesh family L6 uses a much reduced number of trailing edge points, while mesh family L7 increases the number of points, but still keeping them less than the corresponding number for the common unstructured mesh family. Finally, the bending angle for the wing leading edge and tip was the same for the AFLCMC meshes.

Table 5. Grid sizes of the unstructured mesh families (millions of cells)

Level	Common Unstructured	AFLCMC Unstructured					
		L1	L3	L4	L5	L6	L7
0	20.4	20.2	20.0	30.9	26.2	13.3	18.1
1	27.8	29.9	29.7	47.3	39.9	19.5	27.4
2	38.1	46.1	45.9	74.9	63.3	30.0	41.1
3	52.0	71.6	71.3	118.3	100.3	46.1	65.1
4	74.2	111.6	111.1	180.3	152.8	73.1	101.8
5		204.7	203.9	306.3	265.0	135.8	188.9
6						182.7	254.9
7						251.4	

Example visualizations of a subset of the mesh families are shown in Fig. 12. The L1 family is very similar to the common unstructured family (above). Family L3 contains only triangles on the surfaces (and tetrahedra in the volume mesh). Family L4 contains surface triangles and quads, and Families L6 and L7 are quad-dominant (similar to L1 and the common unstructured family), but do not have trailing edges that are refined. L6 trailing edges are coarsened more than L7 trailing edges. Figure 13 compares the trailing edges of the common unstructured mesh and Families L3, L6 and L7. The highly refined trailing edges of the common unstructured meshes are also apparent when

comparing the number of cells in Families L6 and L7 (which have more coarse trailing edges) with Family L3 (which has trailing edge spacings similar to the common unstructured family) – all other spacing constraints between these families are constant.

Table 6. Mesh characteristics of the AFLCMC unstructured mesh families

Mesh Level	Bending Angle	Wall Spacing	Growth Rate	Points Across TE			Viscous Layers
				L1-L5	L6	L7	
0	15	1.3300E-04	1.200	17	5	9	56
1	13.04	1.1565E-04	1.172	19	5	11	64
2	11.34	1.0062E-04	1.148	23	7	11	74
3	9.86	8.7480E-05	1.127	25	7	13	85
4	8.58	7.6050E-05	1.110	29	9	15	98
5	7.46	6.6125E-05	1.095	35	11	19	113
6	6.48	5.7500E-05	1.082		11	21	130
7	5.64	5.0000E-05	1.071		13		149

The wing tip details for the entire L7 family of meshes is shown in Fig. 14. Compared to the common unstructured mesh family, the trailing edges are not as refined. But, as the mesh levels increase (and the meshes are further refined), the trailing edge refinement exceeds that of the common unstructured family, while the surfaces are more refined than the most refined mesh in the common unstructured family.

Mesh naming, such as Tiny, Coarse, etc, are not used for the AFLCMC mesh families due to the number of mesh levels. However, the first level mesh spacings correspond with the Tiny level; therefore, the AFLCMC Level 0 meshes are comparable with the common unstructured Tiny mesh. Similarly, Level 1 compares with Coarse; Level 2 compares with Medium, etc. Nevertheless, there are differences in the numbers of cells between the AFLCMC families and the common unstructured meshes, thus there is some difference in the way in which each mesh level was scaled compared with the previous level.

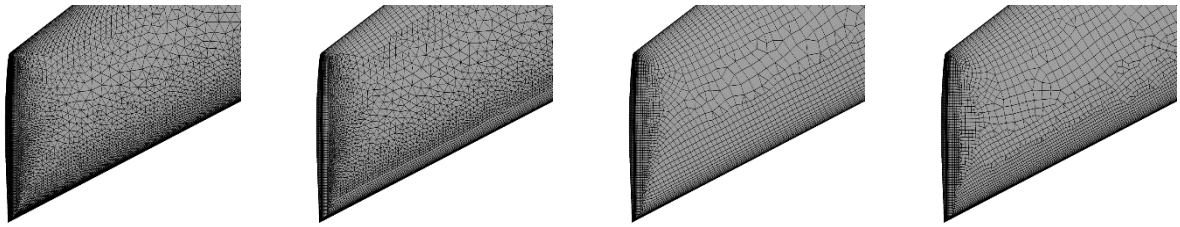

Figure 12. Examples of AFLCMC Unstructured Mesh Families. L3: tri-dominant (far left), L4: hybrid tri and quad (left), L6: quad-dominant with coarsened trailing edge (right), L7: quad-dominant with more refined trailing edge (far right).

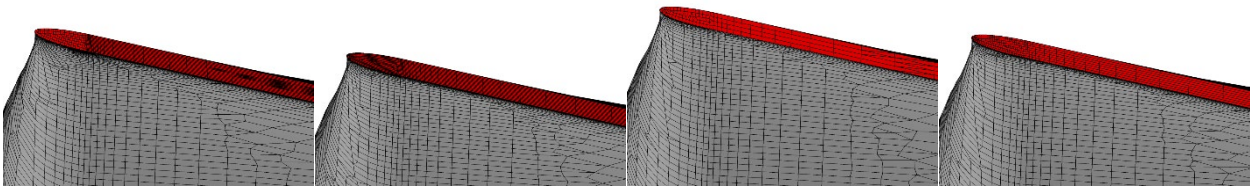

Figure 13. Detail of wing tip showing trailing edge (red) refinement for the Common Unstructured mesh (far left), AFLCMC L3 (left), L6 (right) and L7 (far right) for the Tiny, or Level 0, meshes.

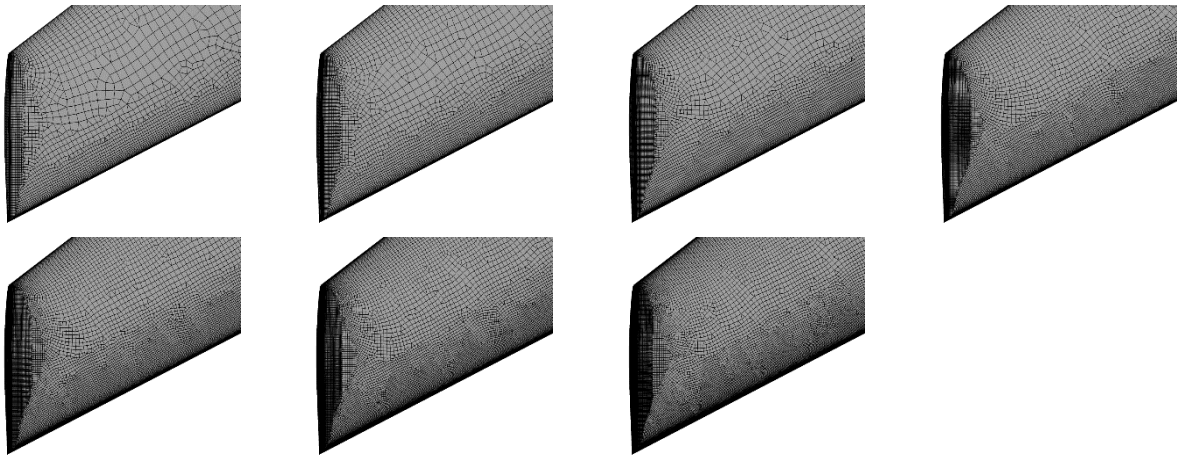

Figure 14. Wing tip details for AFLCMC Family L7. Level 0 (upper far left), Level 1 (upper left), Level 2 (upper right), Level 3 (upper far right), Level 4 (lower far left), Level 5 (lower left), Level 6 (lower right).

- NASA Langley Research Center Grids

Participants from the NASA Langley Research Center generated a series of computational grids using HeldenMesh™ [40] v3.03, a grid generation software system developed by Helden Aerospace Corporation for efficiently generating three-dimensional, mixed-element unstructured meshes of complex configurations. The HeldenMesh™ [40] software consists of two tools, HeldenPatch™ [40] and HeldenMesh™ [40]. HeldenPatch™ [40] is the interface between the Initial Graphics Exchange Specification (IGES) geometry and HeldenMesh™ [40] grid generator that provides geometry clean-up, management, and transformation capabilities. The HeldenPatch™ [40] software is capable of automatic surface patching with limited user-intervention required. HeldenMesh™ [40] utilizes automated advancing-layers and advancing-front unstructured grid generation methods. A simple, text-based input file allows the user to control the spatial resolution of surface grid cells for each unique geometry component, as well as the viscous boundary layer growth rate and options for flow-feature resolution, e.g., wakes and shocks, in the volume domain.

A series of hybrid unstructured grids were generated on the ONERA LRM Configuration with the sting to match the coarse, medium, and fine refinement levels, in terms of number of nodes, for comparisons to the workshop-provided grids. This secondary set of unstructured grids was generated after observing lateral grid asymmetries in the workshop provided grids to better assess any potential impact on the predicted lateral stability derivative values. In support of this, the HeldenMesh™ [40] grids were generated by first creating a semispan domain and mirroring it about the configuration's symmetry plane. Characteristics of the grids are detailed in Table 7, where a global refinement factor, r_{FAC}, within HeldenMesh™ [40] was manually adjusted to produce grids with 21.1, 29.1, and 39.6 million total nodes for participants using node-based CFD solvers. Additionally, a medium refinement grid was generated for the ONERA LRM Configuration without the sting to assess sting increments on static longitudinal stability.

The near-wall, first-node spacing (δ_1) for the coarse grid was specified to match the initial spacing used in the coarse workshop grid. Beyond the first layer of prism cells, the advancing layers (i) grow into the volume domain based on a two-variable stretching factor (r_1 and r_2) equation as defined by

$$\delta_{i+1} = \delta_i * [1 + r_1 * (1 + r_2)^i]^i$$

The global refinement factor within HeldenMesh™ [40] was used to linearly scale the spatial resolution of the grid surface cells and the viscous volume domain normal to the configuration surface. A NASA internal boundary layer refinement tool was used to calculate the boundary layer growth stretch factors, such that the total boundary layer height could be maintained across each level of grid refinement while changing the boundary layer resolution. The refinement and boundary layer stretch factors were iteratively changed until the target number of grid nodes was reached for each level of refinement. Volume domain resolution is shown in Fig. 15 for the series of HeldenMesh™ [40] grids using illustrations of the symmetry plane and a chordwise sectional cut taken at the vehicle moment center. Examples of surface grid resolution for the HeldenMesh™ [40] grids is shown in Fig. 16 using three- and top-views.

Table 7. Grid characteristics for HeldenMesh™ [40] unstructured grid series.

Grid	r_{FAC}	r_1	r_2	δ_1 (in)	Surf. Tri (million)	Tets (million)	Pyramids (million)	Prisms (million)	Cells (million)	Nodes (million)
Coarse	1.08	0.181	0.015	1.14E-4	1.4	24.7	0.2	33.0	57.9	21.1
Medium	0.90	0.140	0.015	9.54E-5	1.6	22.2	0.3	49.8	72.2	29.1
Fine	0.68	0.082	0.015	7.16E-5	1.9	18.6	0.3	71.7	90.6	39.6
Medium w/o Sting	0.90	0.140	0.015	9.54E-5	1.4	18.9	0.2	42.7	61.8	25.0

The minimum surface spacing, nominal surface spacing, maximum stretching ratio, and maximum facet curvature angle was uniquely set for each vehicle component. For the baseline coarse grid, the fuselage and sting were prescribed to have nominal and minimum surface spacings of 5 in. and 0.025 in., respectively. The wing, horizontal tail, vertical tail, and strut all had identical grid resolution with a nominal spacing of 1 in. and a minimum surface spacing of 0.005 in. The trailing edges of the wing and tail components was set to achieve approximately 5 node layers across each surface. For each geometry component, the maximum facet curvature angle was set to 3 degrees to better resolve highly curved surface areas subject to the minimum surface spacing constraint. The maximum cell stretching ratio was set to 10 for the fuselage and sting and 7.5 for the wing, tail, and strut components. Increased cell stretching on the fuselage and sting allows for a larger proportion of the total grid nodes to be created on the lifting wing and tail surface that are more critical for CFD aerodynamic predictions.

VII. Results and Discussion

Results were submitted by twelve participant groups, with some groups submitting multiple sets of results using different turbulence models or grid systems. A total of twenty-one datasets were received. Of these, eight used NASA's FUN3D[41], six used the CREATE Kestrel[42] code and four used NASA's Overflow[43]. The remaining three used Boeing's BCFD[44], DLR's TAU[45], and JAXA's FaSTAR[46] codes. The key to determine the parameters for each run from the abbreviations used in the figures and text is provided in Fig. 17. The common structured and unstructured grids are the original grid systems provided by the workshop. H# and L# are grids generated at the NASA Langley Research Center and the Air Force Research Lab, respectively. Details on the turbulence model and variants can be found in Ref. 36. In short, the negative version of the Spalart-Allmaras (SA) turbulence model includes a modification to improve performance when under-resolved grids are used, the Rotation Correction is a rotation/streamline curvature correction that improves the prediction of vortical flows and the Quadratic Constitutive Relation model version uses a quadratic rather than linear relationship between the flow shear and eddy viscosity. One set of results were obtained using the Mach numbers that were not corrected for the wind tunnel sting (UC) for Cases 2, 4 and 6 (all results used the uncorrected Mach numbers for Case 3). For one set the unsteady version of the governing equations was solved (T) and for another, the component grids were prevented from being split to improve the parallel processing load balance (N).

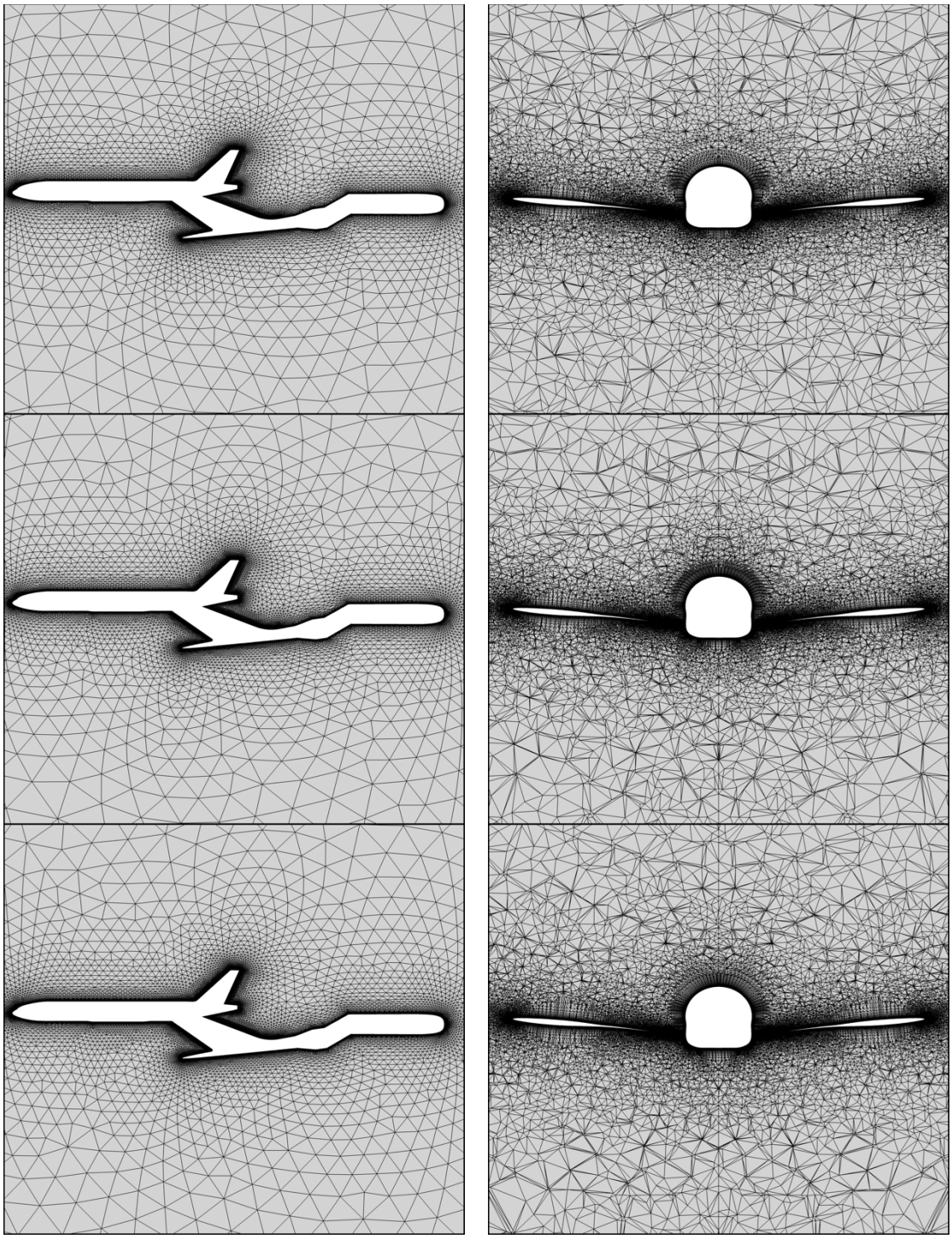

Figure 15. Symmetry plane (left) and moment center sectional plane (right) views of HeldenMesh™ 40 unstructured grid series resolution for the coarse (top), medium (middle), and fine (bottom) refinement levels.

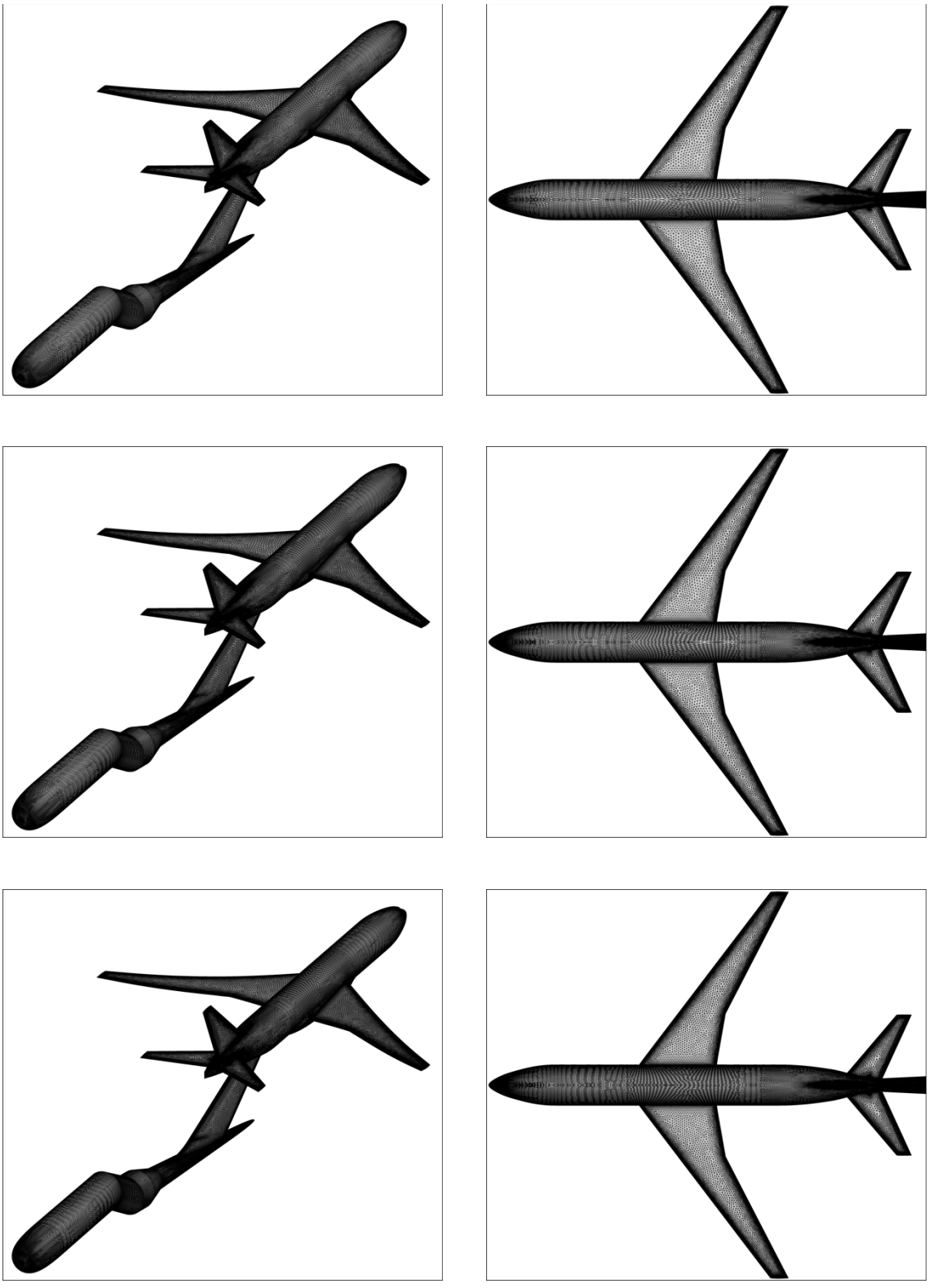

Figure 16. Three-view (left) and top view (right) of HeldenMesh [TM 40] unstructured grid series resolution for the coarse (top), medium (middle), and fine (bottom) refinement levels.

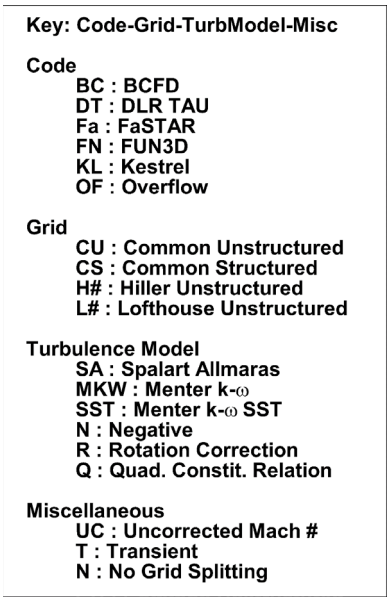

Figure 17. Key for data descriptor.

A. Case 2: Grid Convergence Study

For Case 2, participants were asked to compute the drag, side force, pitching moment, yawing moment, and rolling moment coefficient for the ONERA LRM with the wind tunnel mounting sting for the coarse, medium, and fine grid refinement levels at $Mach = 0.83$, $Re_{MAC} = 4.56$ million, $\beta = 1°$, and $C_L = 0.5$ +/- 0.0001 with the intent of assessing grid convergence. At the same conditions, the angle of attack based on the wind tunnel data was estimated to be 2.94°. For each coefficient, computational results are plotted versus grid factor, $1/N^{2/3}$, where N is the number of grid points. Participants had the option of also submitting data for the Tiny and Extra Fine refinement levels, in addition to any additional refinements available for custom grids. In accordance with the standard Richardson extrapolation method, grid refinement is deemed sufficient when the computational solutions demonstrate asymptotic convergence, which is observed when the solution decreases in error toward a linear fit with increased grid refinement (for a second order accurate spatial scheme given our definition of the grid factor). Extension of this solution fit to the y-intercept then represents the theoretical computational result for an infinitely resolved grid at the condition of interest. The grid convergence results for lift, drag, side force, pitching moment, rolling moment, and yawing moment coefficients from all participant solutions are provided in Figs. 18, 19, 21, 23, 25 and 27, respectively. For these results, the aerodynamic coefficients are decomposed into total, fuselage, port wing, starboard wing, and tail components to better assess their individual grid factor trends. Additionally, histogram plots of the normalized deviation relative to the wind tunnel test (WTT) data (100(CFD-WTT)/WTT) for each total aerodynamic coefficient are provided in Figs. 20, 22, 24, 26 and 28. In each plot, the y-axis is the number of participant predictions for each deviation bin given on the x-axis.

In Fig. 18, the total lift coefficient confirms the general agreement among the participants to achieve the target lift coefficient value of 0.5 within the tolerance of $1/10^{th}$ of a lift count. The lift coefficient decomposition into the individual configuration components shows increased variability relative to the total aerodynamic coefficient. Extrapolation of the results toward the theoretical infinitely resolved solution generally shows approximately a 1-count variation in lift coefficient for the fuselage (CL_FUS), port wing (CL_PWING), and starboard wing (CL_SWING) components except for the Overflow structured grid data that were unable to match the target lift coefficient. In contrast, the data for the lift contribution of the tail (CL_TAIL) show greater variability with the bulk of the participant data falling within a 1 to 2 lift-count range. Overall, the grid factor trends show that a grid factor of 5E-06 or less resembles asymptotic convergence for the component lift coefficient contributions.

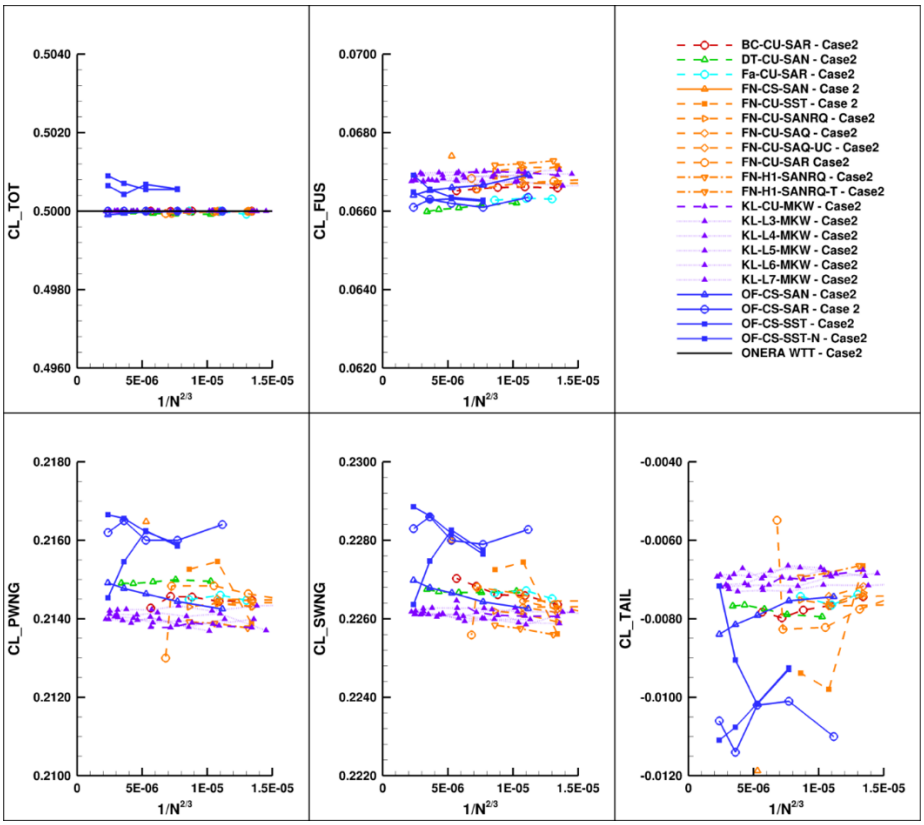

Figure 18. Convergence of lift coefficient with grid size. Mach = 0.83, C_L = 0.5.

The drag coefficient decomposition for the configuration and individual components is shown in Fig. 19. In contrast to the total lift coefficient, the total drag coefficient shows greater variability with a 20 to 30 drag-count range at all grid refinements. Furthermore, the grid factor trend only begins to trend toward a linear variation at the finest grid refinement levels, suggesting that grid resolution for the participant grids may not be sufficient to achieve asymptotic convergence. However, the component drag coefficients show reduced variability with approximately an 8 drag-count range for the fuselage and wings, whereas the tail shows a tighter range of around 4 drag-counts for each grid refinement level. The grid factor trend for the tail component indicates that increased grid resolution may still be needed to reach the asymptotic convergence region. Given that the test case condition is at a positive sideslip angle, this may indicate the need for feature-based grid adaptation/resolution to resolve possible vortex shedding about the vertical tail component. Reviewing the histogram of the drag coefficient results in Fig. 20. shows a negative bias toward underprediction of the drag coefficient when using the SA turbulence model, for both structured and unstructured grids, and an overprediction of the drag coefficient when using the k-ω turbulence model. Overall, the results show an approximately normal distribution about the wind tunnel data with most of the results falling within the bounds of -4 to 4 percent deviation relative to the wind tunnel data.

Figures 21 and 22 show the grid convergence and histogram plots for side force coefficient, respectively. Generally, most of the data shows limited variation with grid refinement and a relatively linear fit of the data for both the total and component contributions. Additionally, the variability of these data is confined to approximately a 10-count range. In contrast to the drag coefficient, the side force coefficient histogram plot shows a negative bias relative to the wind tunnel data with a bulk of the data underpredicting the side force coefficient by 2 to 6%.

Figure 23 provides the grid convergence results for pitching moment coefficient. Relative to the previous aerodynamic coefficients, the total pitching moment coefficient data shows significant variability with up to a 150-count difference for the lift-matched solutions. In terms of grid convergence, most solutions show a nonlinear variation in pitching moment at the finest grid refinement levels (lowest grid factor), indicating that the participant grids may be under resolved to predict the flow features at the noted test case condition. In reviewing the pitching moment coefficient at the component level, it is apparent that the tail contributes the largest variability to the total pitching moment coefficient relative to the fuselage and wing components. This observation is similar to that of the side force coefficient, which reinforces the idea that feature-based grid refinement and/or additional refinement of the tail may

be necessary to generate grid independent solutions at non-zero sideslip angles. The histogram plot of the pitching moment data, shown in Fig. 24, indicates a general bias of the CFD solutions toward overpredicting pitching moment coefficient by 10 to 50% when compared to the wind tunnel data.

The grid convergence results for the total and component rolling moment coefficients are illustrated in Fig. 25. The total rolling moment coefficient shows limited variability with only a 2-count range across all grid refinement levels. In terms of grid convergence, the participant data generally show a linear fit for grid factors below 7E-06. At the component level, the fuselage and tail rolling moment coefficient data had favorable agreement across all solutions and grid refinement levels with limited variability. In contrast, the port- and starboard-wing components showed a more significant variability with a 5 to 6-count range in the rolling moment data. Furthermore, the variation with grid factor also shows a generally nonlinear trend with the implication that further grid refinement may allow for improved solution accuracy. The histogram plot of rolling moment error is shown in Fig. 26. The rolling moment error is observed to have a slightly negative bias relative to the wind tunnel data with most of the solution data showing accuracy within -4 to 2%.

Figures 27 and 28 provide the grid convergence and histogram results for the yawing moment coefficient. Overall, the total yawing moment coefficient is shown to be in favorable agreement with only a few counts of difference among all participant data and grid refinement levels. Additionally, the grid factor trend shows a relatively linear fit that suggests the grids are in the asymptotic convergence region in terms of resolving the yawing moment coefficient. For the lift-matched solutions, these qualitative features are generally observed for each of the individual configuration components with a tight range of pitching moment values across all grid refinement levels. The histogram results show a wider spread in normalized deviation relative to the wind tunnel data when compared to the other aerodynamic coefficients. Overall, the participant data are biased toward underpredicting the yawing moment coefficient with the observation that the structured grid results tended to have more prediction error relative to the unstructured grids (recall that the improved structured overset vertical tail grid was not available for the grid refinement study).

In summary, the results of the grid convergence study reflected a general agreement between the participant data for the force and moment coefficients except for significant variability in the pitching moment coefficient, as noted by the 10 to 50% overprediction relative to wind tunnel data. At the component level, the tail component was shown to contribute more significantly to the variability in total pitching moment coefficient. Nonetheless, state-of-the-art CFD predictions have historically had challenges in predicting pitching moment coefficient. Overall, the grid factor trends generally showed that the asymptotic grid convergence region could be achieved for grid factors less than approximately 6E-06. Relative to the workshop provided grids, this corresponds to the medium grid refinement level for cell-centered solvers and was the recommended grid refinement level for all subsequent test cases

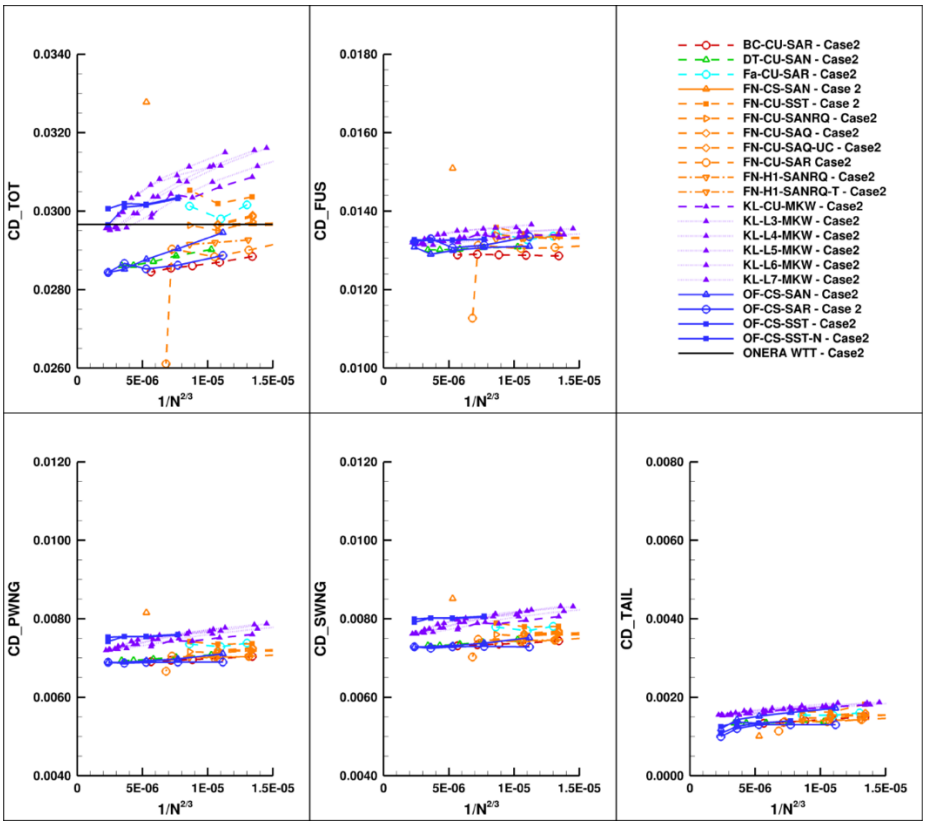

Figure 19. Convergence of drag coefficient with grid size. Mach = 0.83, C_L = 0.5.

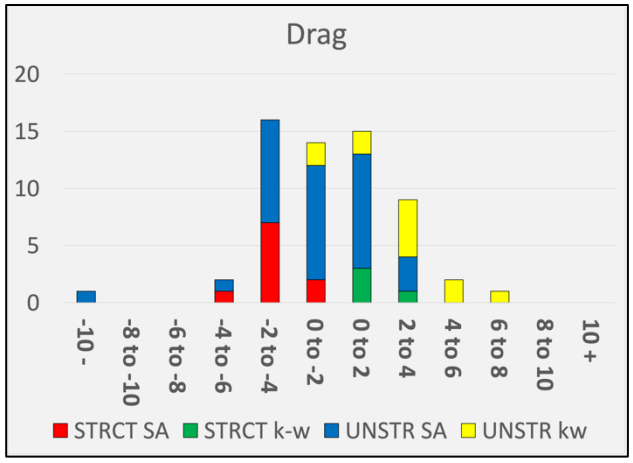

Figure 20. Histogram of the normalized deviation relative to the wind tunnel test data (100(CFD-WTT)/WTT) for drag coefficient from all Case 2 results. Mach = 0.83, C_L=0.5. The y-axis is the number of participant predictions for each deviation bin given on the x-axis.

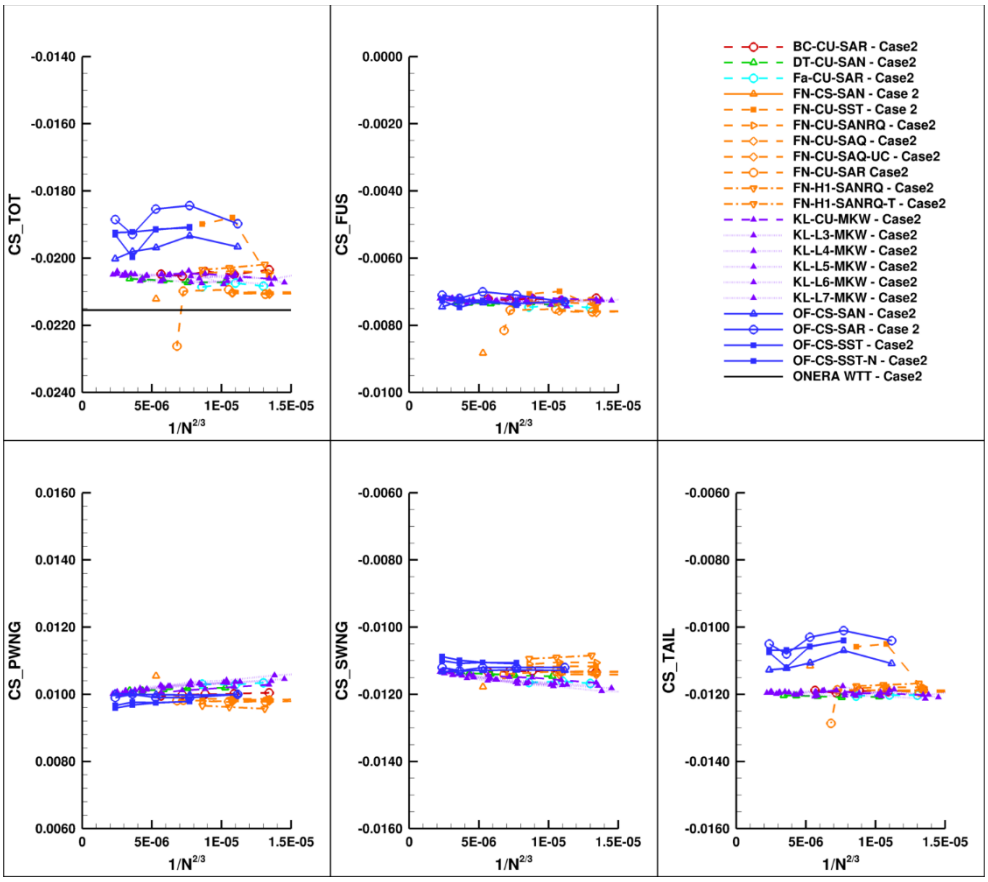

Figure 21. Convergence of side force coefficient with grid size. Mach = 0.83, C_L = 0.5.

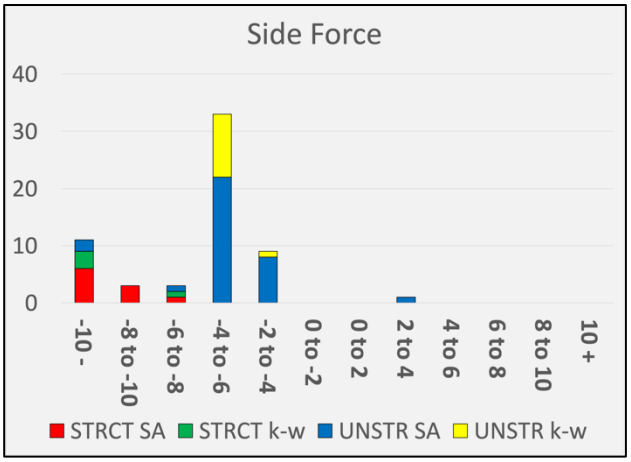

Figure 22. Histogram of the normalized deviation relative to the wind tunnel test data (100(CFD-WTT)/WTT) for side force coefficient from all Case 2 results. Mach = 0.83, C_L=0.5. The y-axis is the number of participant predictions for each deviation bin given on the x-axis.

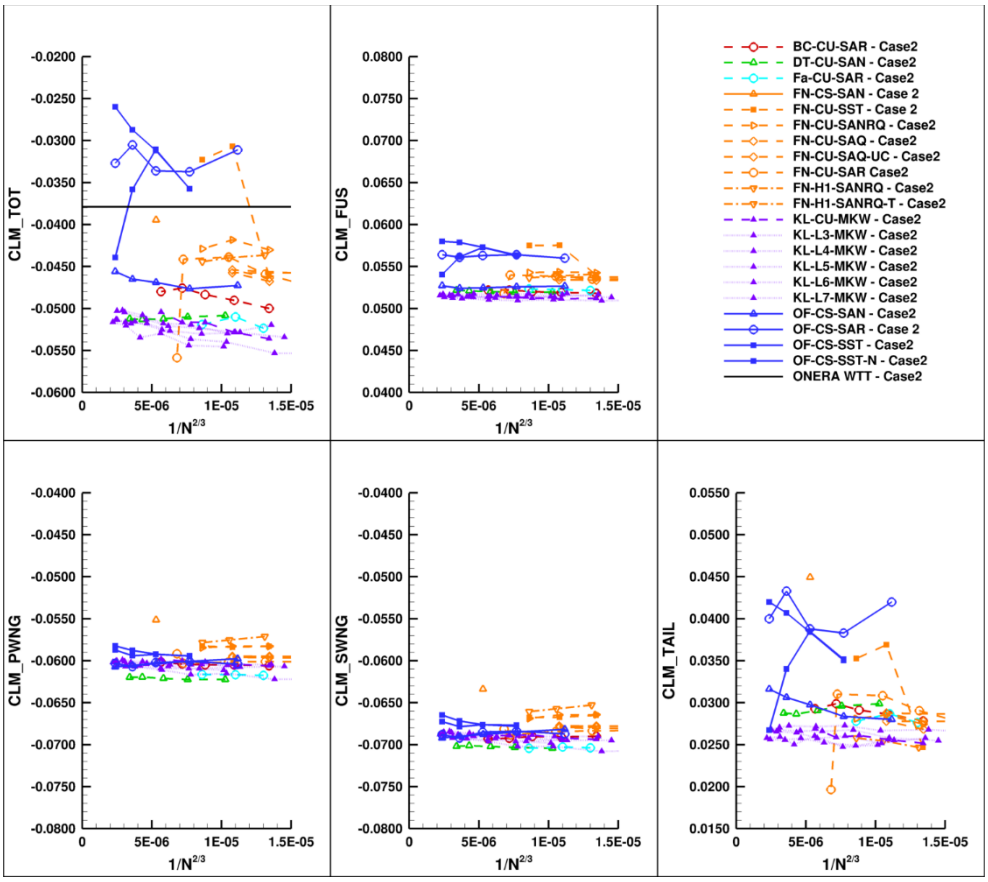

Figure 23. Convergence of pitching moment coefficient with grid size. Mach = 0.83, C_L = 0.5.

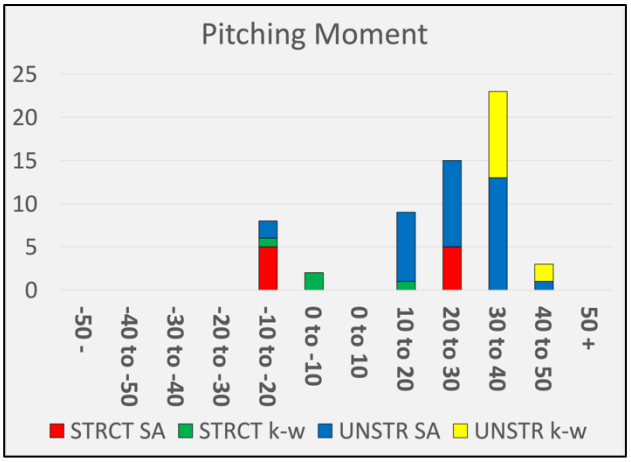

Figure 24. Histogram of the normalized deviation relative to the wind tunnel test data (100(CFD-WTT)/WTT) for pitching moment coefficient from all Case 2 results. Mach = 0.83, C_L=0.5. The y-axis is the number of participant predictions for each deviation bin given on the x-axis.

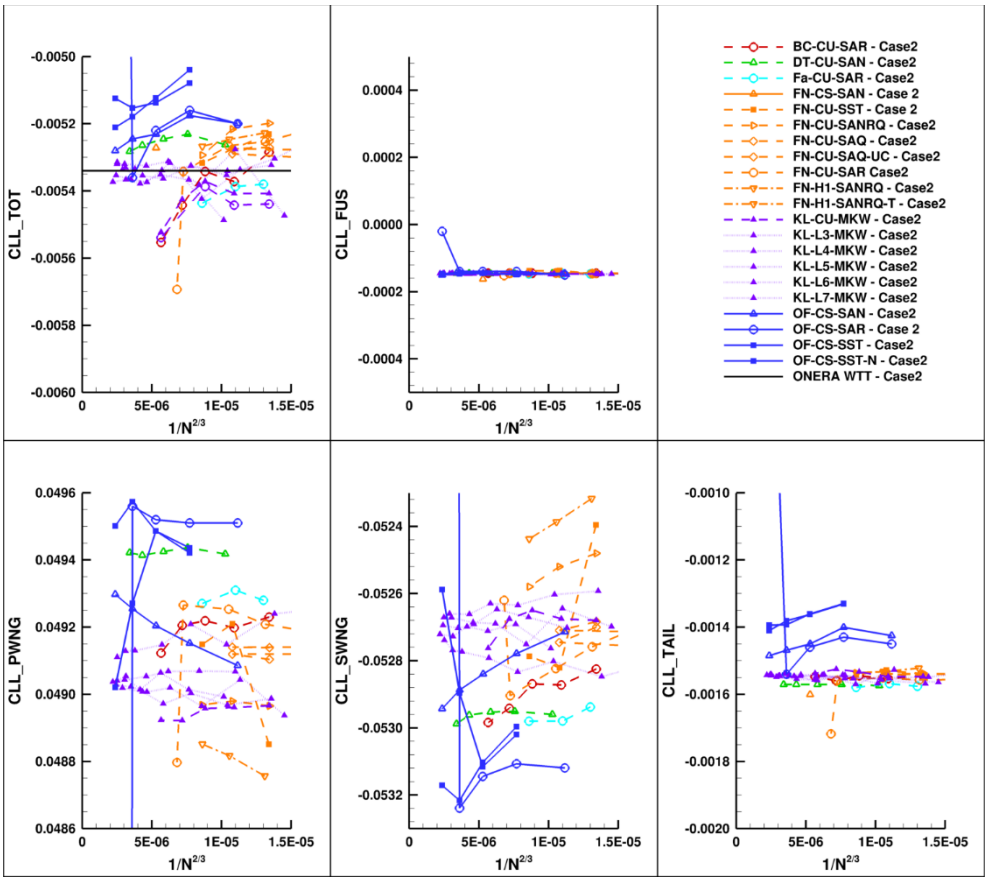

Figure 25. Convergence of rolling moment coefficient with grid size. Mach = 0.83, C_L = 0.5.

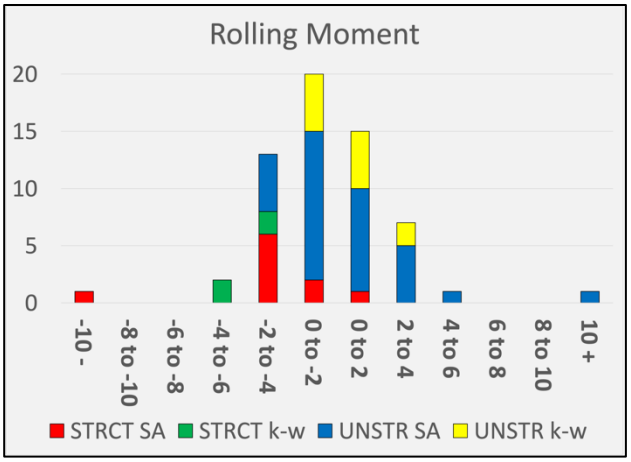

Figure 26. Histogram of the normalized deviation relative to the wind tunnel test data (100(CFD-WTT)/WTT) for rolling moment coefficient from all Case 2 results. Mach = 0.83, C_L=0.5. The y-axis is the number of participant predictions for each deviation bin given on the x-axis.

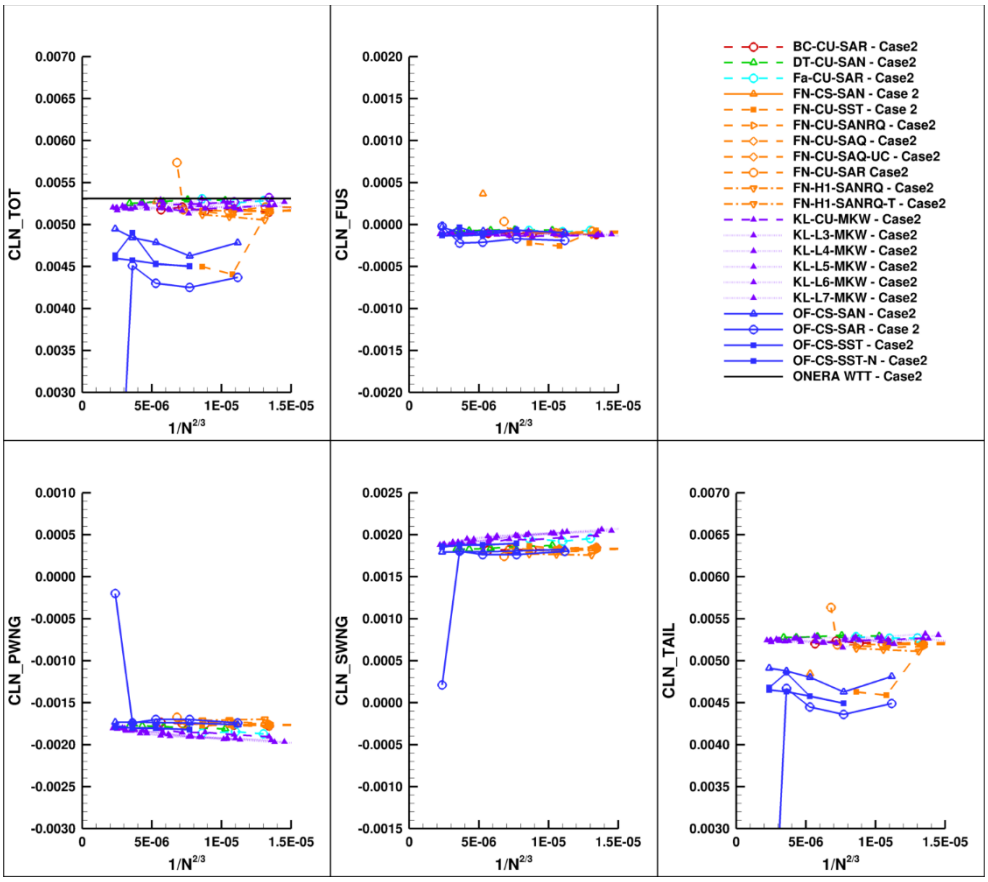

Figure 27. Convergence of yawing moment coefficient with grid size. Mach = 0.83, C_L = 0.5.

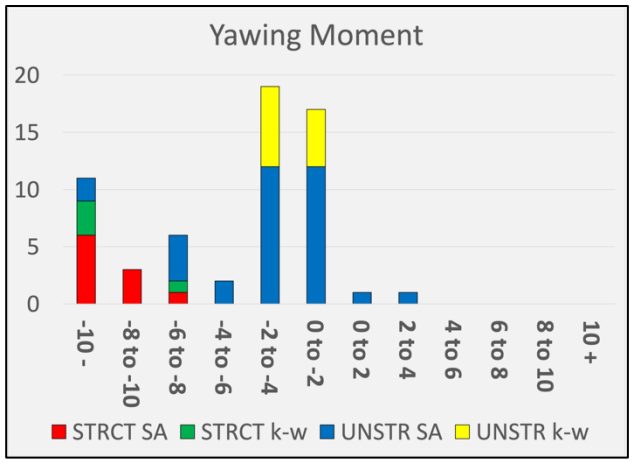

Figure 28. Histogram of the normalized deviation relative to the wind tunnel test data (100(CFD-WTT)/WTT) for yawing moment coefficient from all Case 2 results. Mach = 0.83, C_L=0.5. The y-axis is the number of participant predictions for each deviation bin given on the x-axis.

B. Case 3: LRM Mach Effect on Static Stability (Rework)

The results for Case 3 (Mach sweep) were re-computed due to two main factors. First, the new simulations used the wind tunnel uncorrected Mach numbers. Second, additional meshes were generated by participants to address

concerns with the committee-provided meshes. Participants were asked to generate new solutions using their solvers on some of the new meshes so that a variety of solutions on each mesh would be presented.

The simulations targeted a constant lift coefficient of 0.5, with the angle-of-attack α floating. Fig. 29 shows the final α and computed integrated force and moment coefficients for each solution as compared with the wind tunnel measurements. In general, the computed α is slightly lower than the measured α, but the computed trends agree well with the experimental data. Also note the tight agreement at lower Mach numbers with additional scatter at higher Mach numbers; this trend will be noted in many of the results that follow. None of the experimental values exactly matched the target lift coefficient of 0.5; therefore, integrated force and moment coefficients for the experiment were obtained by interpolating between the two experimental data points that corresponded to the lift values just over and under the target lift value.

Lift shows that most of the simulations achieved the target lift coefficient with very little scatter, although there are a couple of outliers. Note that the OVERFLOW solution resulted in slightly higher lift values at the higher Mach numbers. This difference may have some significance when comparing the surface pressure values below. There is also a high degree of agreement for drag at the low Mach numbers, with increasing scatter at higher Mach. All simulations under predict the drag at the highest Mach, although one FUN3D prediction is close. In general, the computational predictions for side force coefficient follow the experimental trends at lower Mach, although the predicted values are slightly higher than measured. The computational results also show some scatter at higher Mach.

Pitching moment coefficient predictions show a high degree of scatter, even at lower Mach, with increasing disagreement at higher Mach. Wind tunnel results show a near-monotonic increase in pitching moment coefficient with increasing Mach. Some computational results mirror this trend, with the exception of the Mach 0.87 case, for which pitching moment coefficient is predicted to decrease. Other computational results predict increasing pitching moment coefficient for increasing Mach at the lower speeds, but then predict decreasing pitching moment coefficient with increasing Mach at the higher speeds. Clearly computational methods struggle to predict pitching moment coefficient values for the LRM configuration at transonic speeds. Rolling moment coefficient predictions are relatively good, with the computational simulations agreeing with each other and wind tunnel results, except for the Mach 0.87 case where some scatter is evident. The computational predictions of yawing moment coefficient agree well with the experimental results, although there are some outliers, and additional scatter at higher Mach (as with side force coefficient predictions). The integrated force and moment coefficients for the individual air vehicle components (fuselage, individual wings, and tail section) from the computed solutions are shown in Figs. 30 through 35, along with the total forces and moments.

As lift coefficient was targeted at 0.5 for each solution, there should be a fair amount of agreement between the CFD solutions. This is the case for lift coefficient due to each wing (which are the major contributors of lift), but there are some differences at the higher Mach numbers for the tails and the fuselage. It's notable that in the case where the lift coefficient on the tails is higher, the lift coefficient on the fuselage is lower to compensate. There is little scatter in the drag coefficient breakdown on the wings, especially at lower Mach, but note the increased scatter of drag coefficient due to the fuselage and tails (even though the tails' drag coefficient contribution is about an order of magnitude lower than that from the wings and fuselage). A similar trend is seen in the side force coefficient contributions, although the contribution by the tails is significantly higher, as expected.

As previously mentioned, the total rolling moment coefficient agrees well with experiment except for the scatter in the Mach 0.87 case. This scatter appears to be equally spread between the wings at the higher Mach numbers. It's noteworthy that total rolling moment coefficient at Mach 0.9 is in good agreement with experiment, but there is a significant amount of disagreement between the contributions due to each wing. Those differences tend to cancel out, giving a good prediction for total rolling moment coefficient.

As mentioned above, most of the computed predictions for pitching moment coefficient do not agree with each other or the experimental data, especially at higher Mach conditions. The component pitching moment coefficient breakdown shows a significant amount of scatter for each of the components, but it appears to be most significant for the fuselage contribution. It's notable that the Kestrel results tend to significantly under-predict the pitching moment coefficient at the higher Mach conditions, which appears to be primarily due to the fuselage and wing contributions. While the tail might have a significant effect on pitching moment coefficient, the tail contributions in the Kestrel solutions tend to be about the same as other solvers. But, for the wings and fuselage, Kestrel's pitching moment coefficient contributions are lower than the others. As will be shown below, this is most likely due to differences in shock location predictions.

The breakdown in yawing moment coefficient contributions shows that the scatter is due mostly to differences due to the tail section. There is a surprisingly little scatter in contributions from the wings. While there appears to be a large amount of scatter in the fuselage contributions, note that the magnitude of yawing moment coefficient due to the fuselage is about one order of magnitude less than that from the tails.

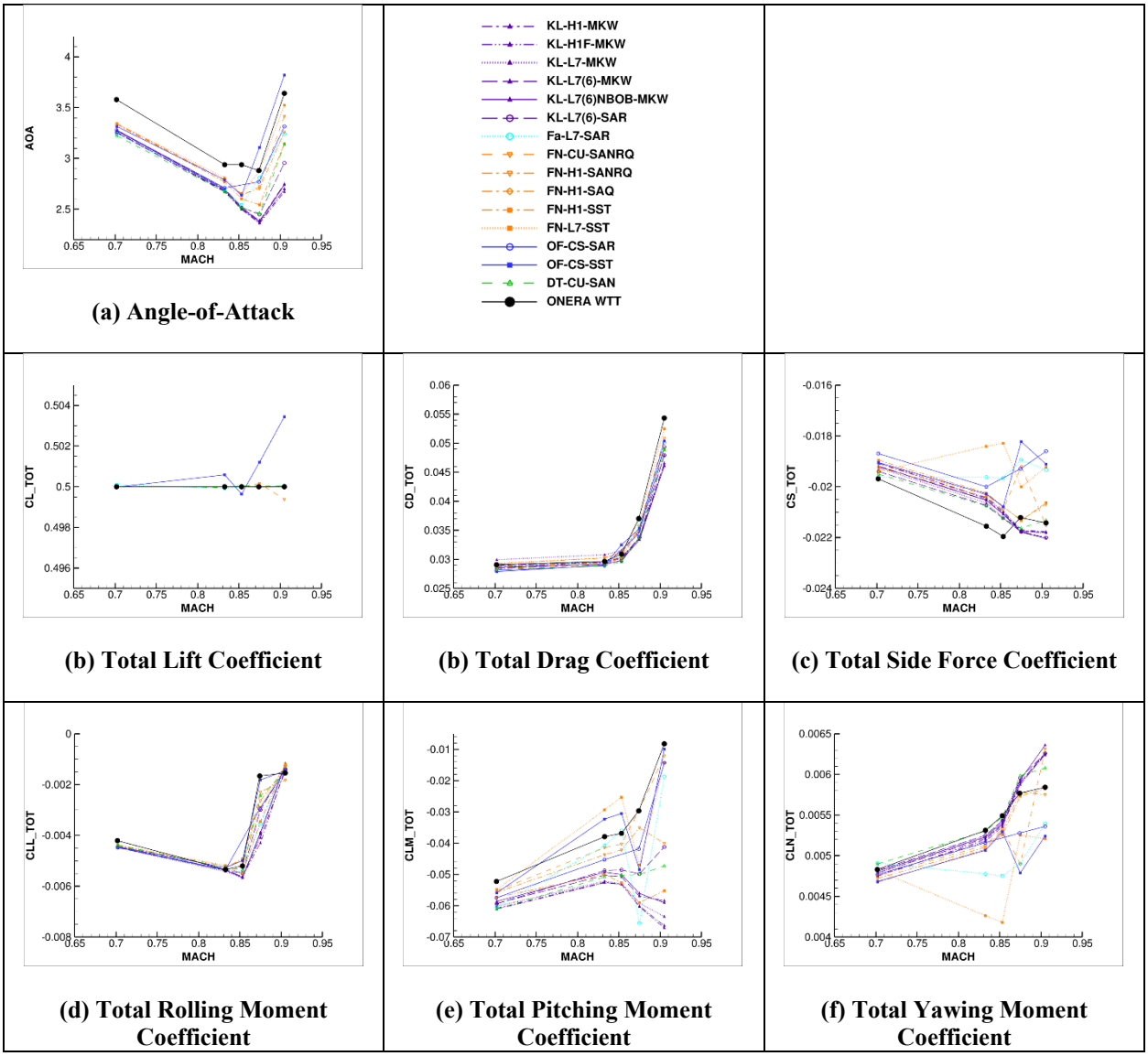

(a) Angle-of-Attack

(b) Total Lift Coefficient

(b) Total Drag Coefficient

(c) Total Side Force Coefficient

(d) Total Rolling Moment Coefficient

(e) Total Pitching Moment Coefficient

(f) Total Yawing Moment Coefficient

Figure 29. Case 3 Rework, Angle-of-attack and integrated force and moment coefficients vs Mach.

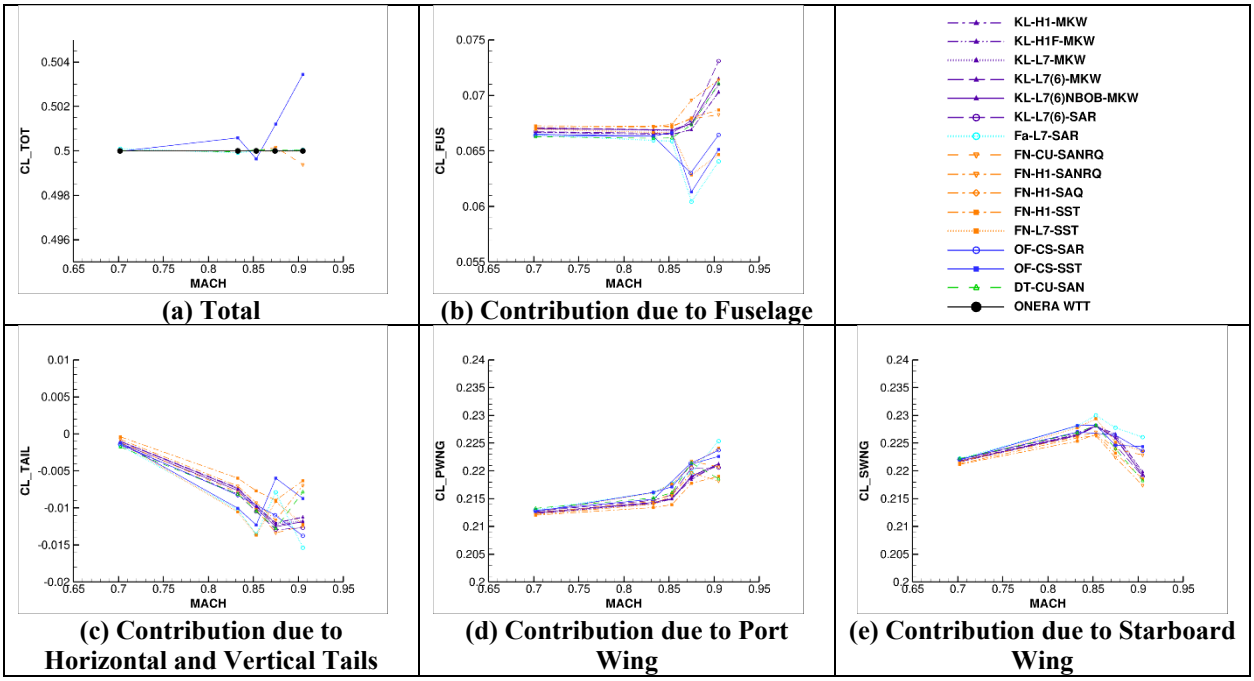

Figure 30. Lift coefficient breakdown by components.

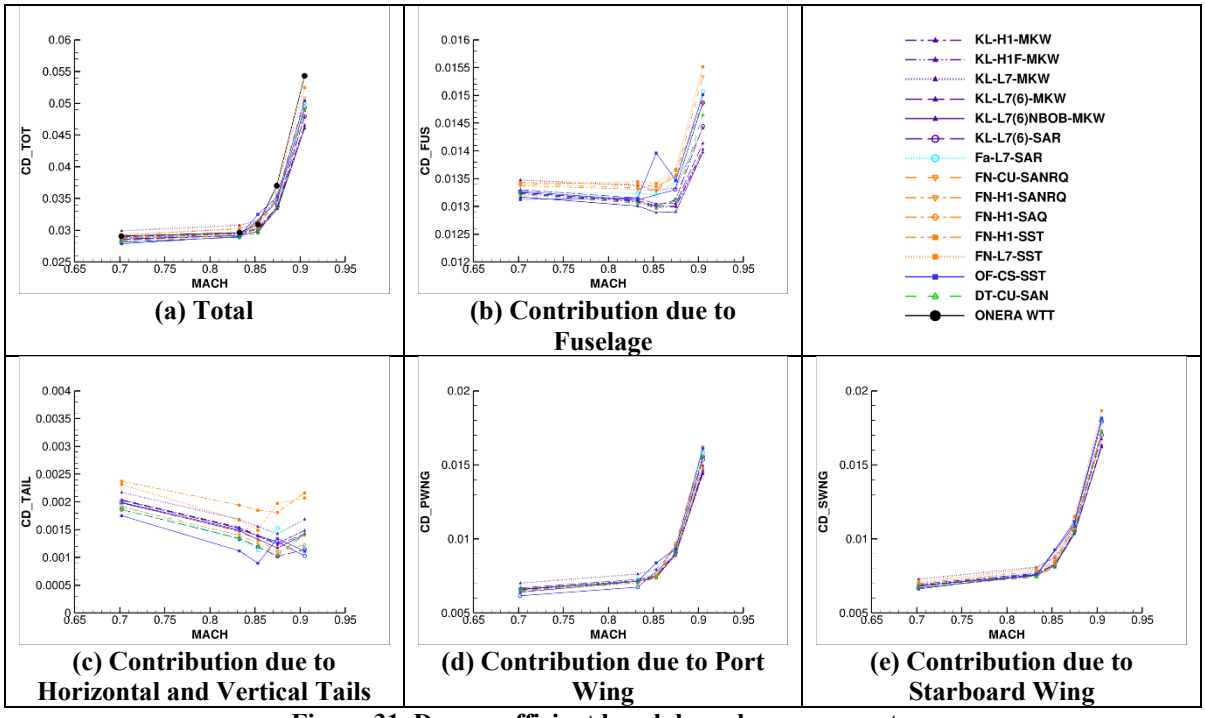

Figure 31. Drag coefficient breakdown by components.

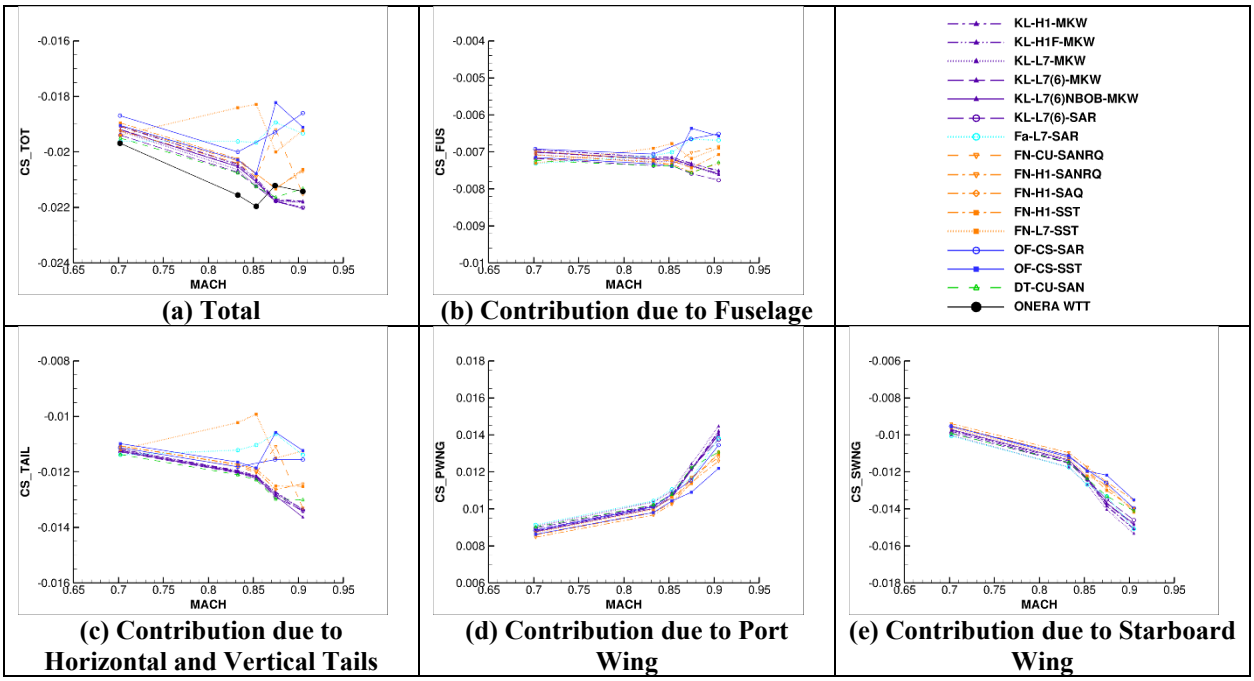

Figure 32. Side force coefficient breakdown by components.

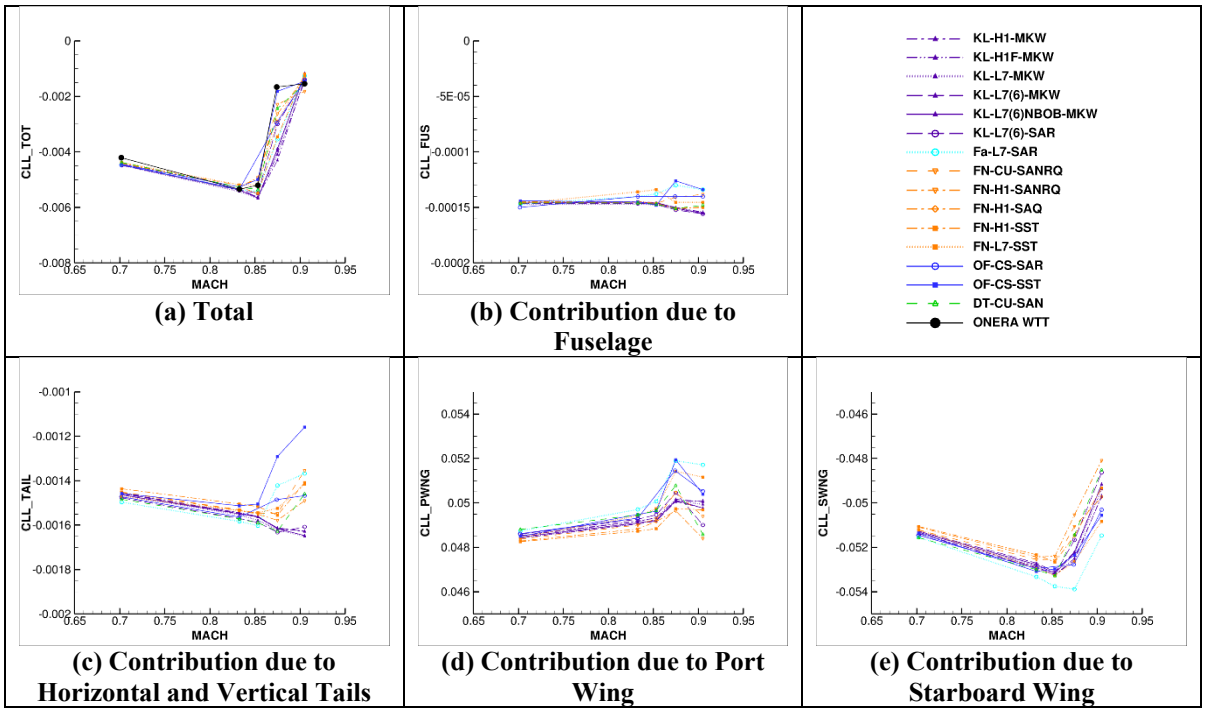

Figure 33. Rolling moment coefficient breakdown by components.

Surface pressure coefficient data from some of the computational results are compared with measured experimental values in the following figures. Five sectional cuts along the starboard wing and one sectional cut on the port wing are shown, along with two locations on the starboard horizontal tail and one on the port horizontal tail. The wing sections are labeled in alphabetical order, with A being near the wing-fuselage juncture and E near the wing tip. As with the integrated force and moment coefficients, none of the experimental conditions exactly matched the target lift coefficient of 0.5. However, instead of interpolating the surface pressure coefficient data from two experimental data points, the surface pressure coefficient data from a single experimental point are plotted with the

computational data. The experimental data correspond to a lift coefficient just over 0.5. The experimental lift coefficient is 0.510 for Mach 0.7, 0.503 for Mach 0.83, 0.513 for Mach 0.85, 0.503 for Mach 0.87, and 0.508 for Mach 0.90. Each experimental lift coefficient value is noted in the plot captions. An example solution from Kestrel using the Spalart-Allmaras turbulence model with the Rotation/Curvature correction (SARC) is also shown in each case.

Computational pressure coefficient data along the different sectional cuts for the Mach 0.7 condition are plotted in Fig. 36. Good agreement between the experimental data and the computational results are seen in all cases. Shocks are not seen in the solution, except perhaps near the leading edge for Wing Sections B and C due to the relatively low Mach number condition. There is also good agreement for the tail sections, although the computational results slightly underpredict pressure on the port horizontal tail and the overpredict pressure on the starboard outer section (G).

Surface pressure coefficient data for Mach 0.83 are compared in Fig. 37. Comparison between the computational and experimental results are reasonable, although there are some differences in the shock locations at the 72% span locations for both the starboard and port wings (Section D). There is also some scatter between the computational results at these locations. The experimental pressure coefficient data on the outboard tail section (G) appears to show equal pressures on top and bottom surfaces, although the computational results show some pressure difference.

Surface pressure coefficient comparisons for Mach 0.85 are shown in Fig. 38. In general, the same trends apply to this case as with Mach 0.83. In general, good agreement between the computational results and the experimental values for the inboard wing and tail sections, but there are differences in the computed shock locations near the outboard wing sections (D and E). There is reason to believe that there are significant unsteady effects in the position of the shock at the mid-span locations (particular Section D) at this Mach. Therefore, the amount of disagreement between the RANS solutions and the experiment is not entirely surprising. Note also the appearance of a shock at the mid-span of the horizontal tail (H).

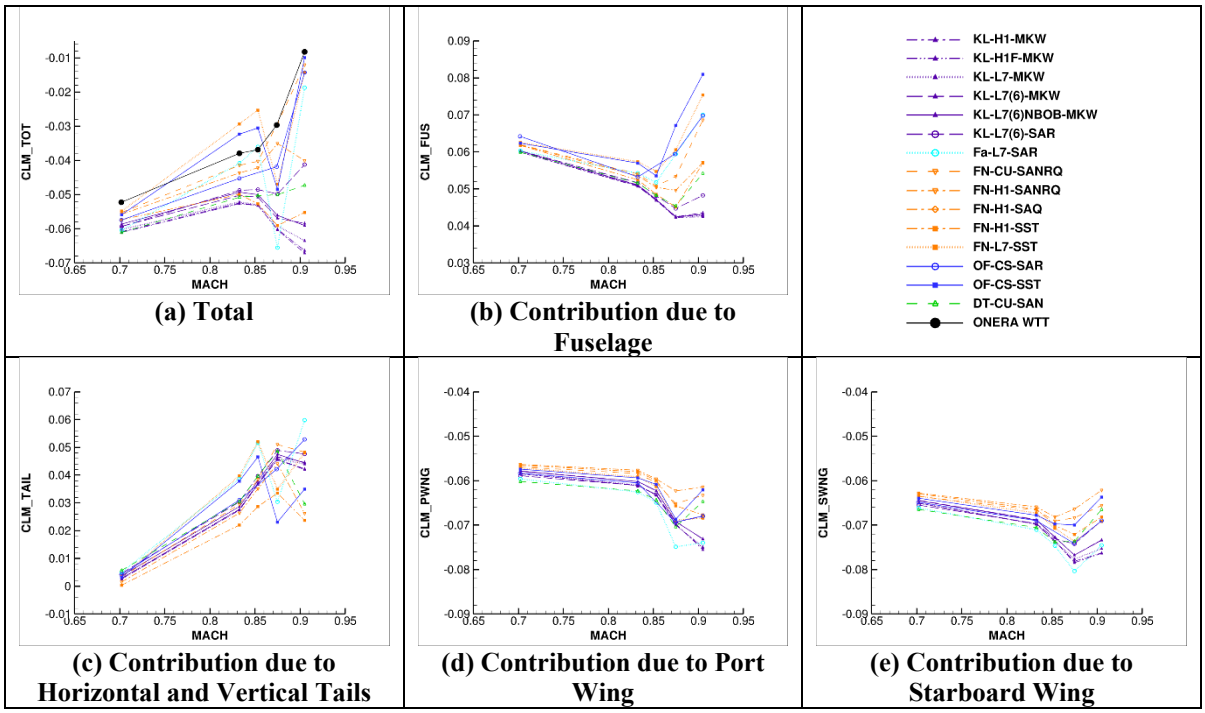

Figure 34. Pitching moment coefficient breakdown by components.

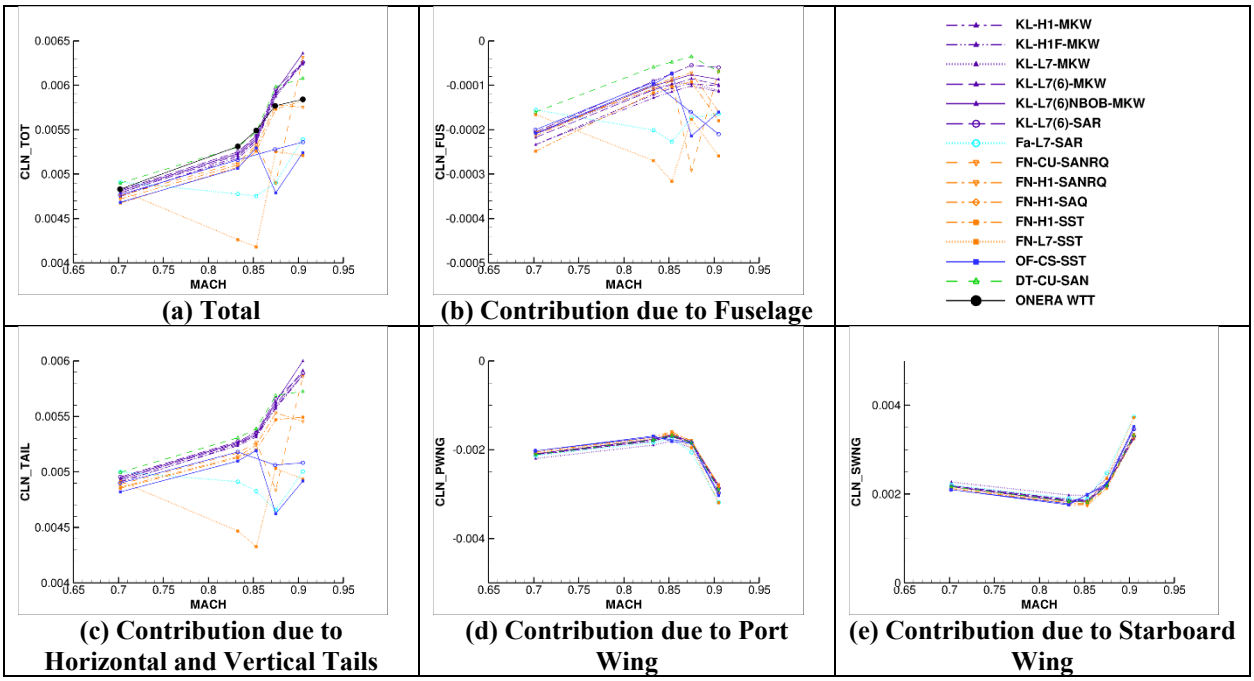

Figure 35. Yawing moment coefficient breakdown by components.

Significant differences are seen in the Mach 0.87 computational solutions, as shown in Fig. 39. Some of the computational solutions (OVERFLOW and FaSTAR) show some smearing of the shock in the inboard wing sections (A and B). All of the outboard wing sections (from C to E) show significant deviations in shock location predictions, with the OVERFLOW solution (plotted in pink) tending to compare best with the experimental pressure distribution at these locations, with FUN3D showing reasonable results as well. Kestrel solutions consistently predict a shock location further aft for Sections C and D, without much difference between solutions that used different meshes or turbulence models. Note also that most of the computational results tend to underpredict the suction pressure at the pre-shock locations, while OVERFLOW slightly overpredicts the suction pressure at these outboard locations. Note also that OVERFLOW and FaSTAR tend to underpredict the suction pressure on the tail sections.

Surface pressure comparisons for Mach 0.90 are shown in Fig. 40. There are significant differences between the computational results, especially near the shocks. Kestrel compares the best for the wing section near the fuselage (Section A), but predicts a shock location further aft of experiment for the outboard wing sections. Again, OVERFLOW tends to compare well with the experimental shock location, although the pre-shock suction pressure is overpredicted. Significant differences are seen for most of the computational solutions on the tail, with the Kestrel simulations comparing best with experiment.

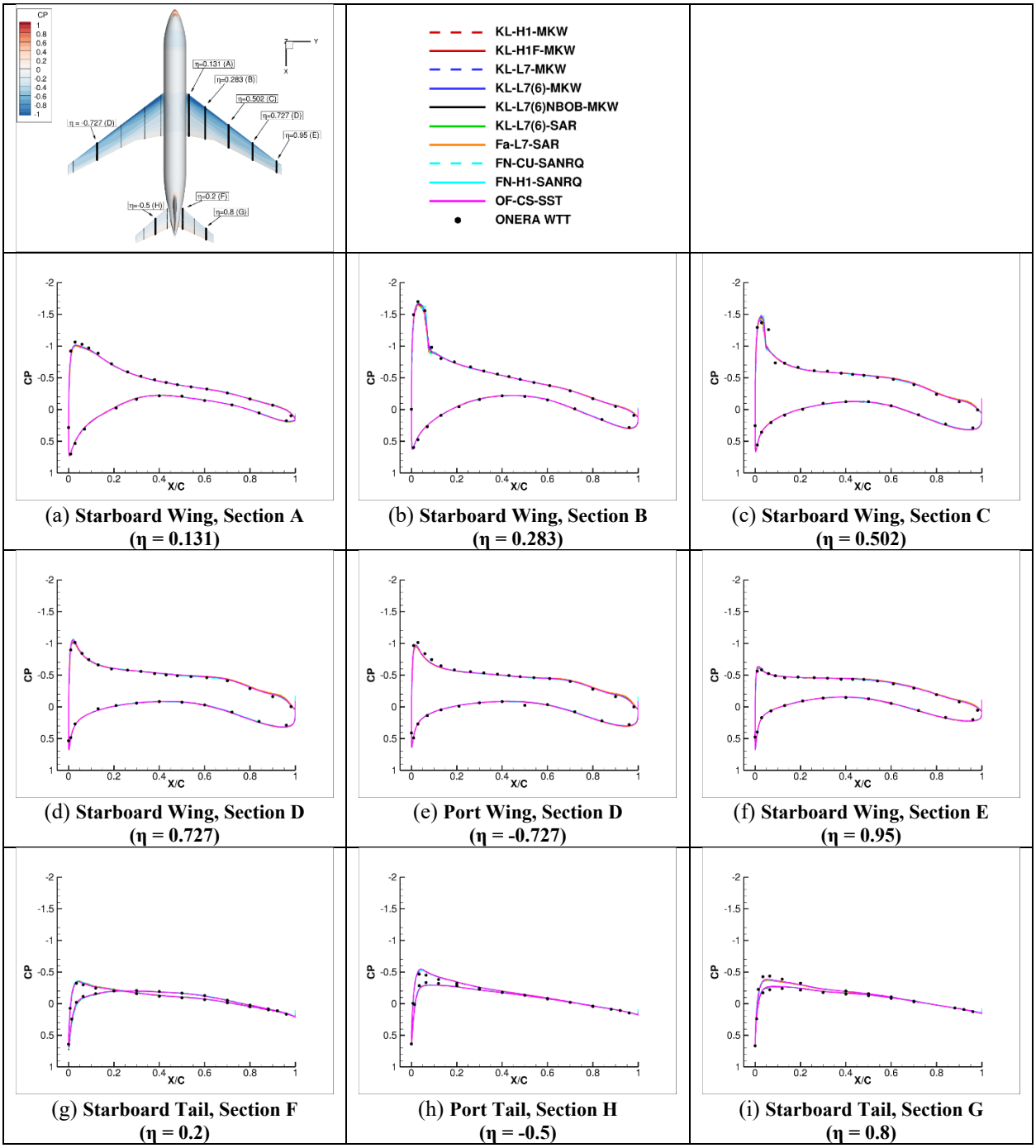

(a) **Starboard Wing, Section A (η = 0.131)**

(b) **Starboard Wing, Section B (η = 0.283)**

(c) **Starboard Wing, Section C (η = 0.502)**

(d) **Starboard Wing, Section D (η = 0.727)**

(e) **Port Wing, Section D (η = -0.727)**

(f) **Starboard Wing, Section E (η = 0.95)**

(g) **Starboard Tail, Section F (η = 0.2)**

(h) **Port Tail, Section H (η = -0.5)**

(i) **Starboard Tail, Section G (η = 0.8)**

Figure 36. Mach 0.70 Surface Pressure Coefficient Cuts (WT C_L = 0.510)

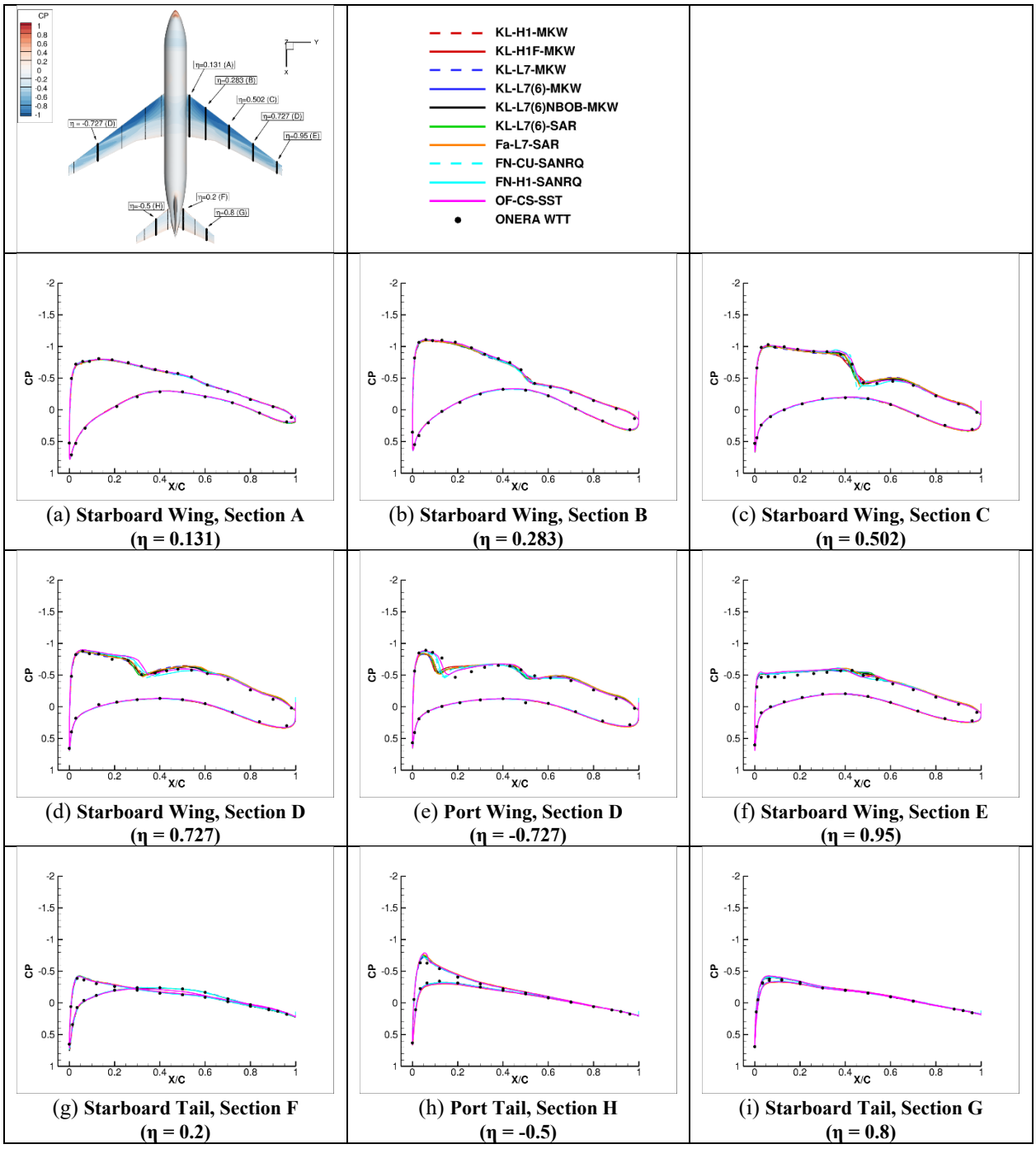

(a) **Starboard Wing, Section A (η = 0.131)**

(b) **Starboard Wing, Section B (η = 0.283)**

(c) **Starboard Wing, Section C (η = 0.502)**

(d) **Starboard Wing, Section D (η = 0.727)**

(e) **Port Wing, Section D (η = -0.727)**

(f) **Starboard Wing, Section E (η = 0.95)**

(g) **Starboard Tail, Section F (η = 0.2)**

(h) **Port Tail, Section H (η = -0.5)**

(i) **Starboard Tail, Section G (η = 0.8)**

Figure 37. Mach 0.83 Surface Pressure Coefficient Cuts (WT C_L = 0.503)

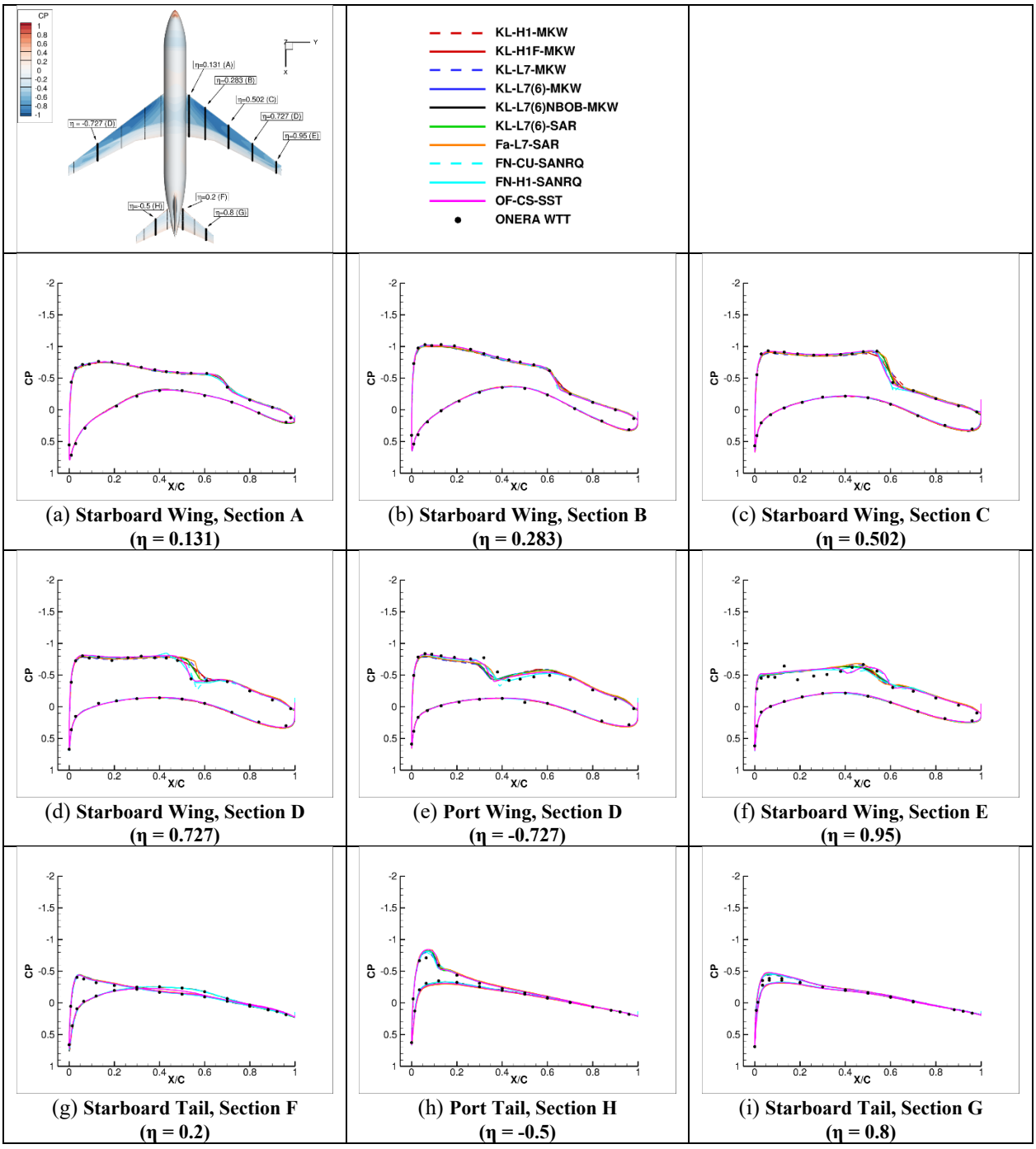

(a) **Starboard Wing, Section A (η = 0.131)**

(b) **Starboard Wing, Section B (η = 0.283)**

(c) **Starboard Wing, Section C (η = 0.502)**

(d) **Starboard Wing, Section D (η = 0.727)**

(e) **Port Wing, Section D (η = -0.727)**

(f) **Starboard Wing, Section E (η = 0.95)**

(g) **Starboard Tail, Section F (η = 0.2)**

(h) **Port Tail, Section H (η = -0.5)**

(i) **Starboard Tail, Section G (η = 0.8)**

Figure 38. Mach 0.85 Surface Pressure Coefficient Cuts (WT C_L = 0.513)

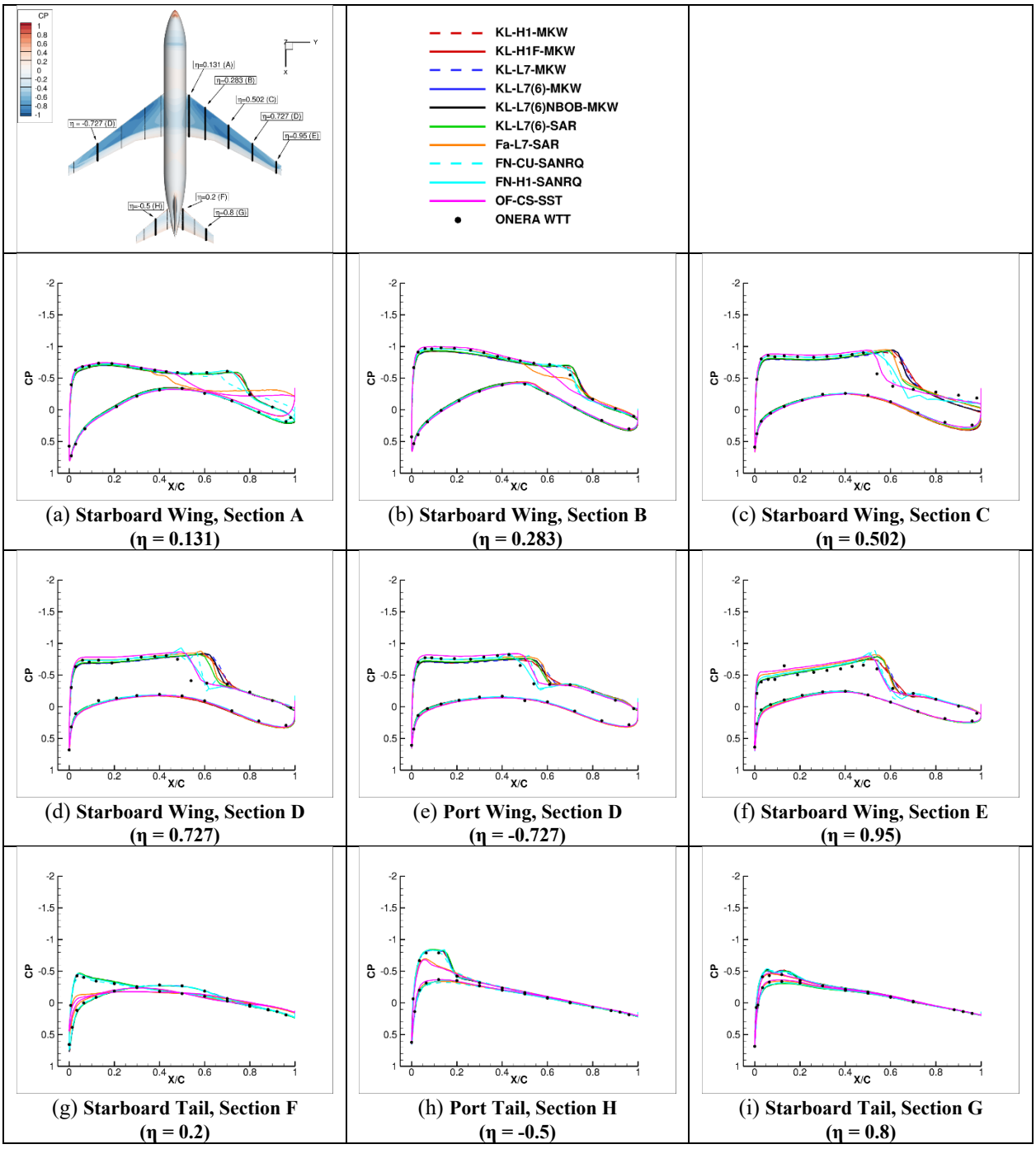

(a) **Starboard Wing, Section A (η = 0.131)**

(b) **Starboard Wing, Section B (η = 0.283)**

(c) **Starboard Wing, Section C (η = 0.502)**

(d) **Starboard Wing, Section D (η = 0.727)**

(e) **Port Wing, Section D (η = -0.727)**

(f) **Starboard Wing, Section E (η = 0.95)**

(g) **Starboard Tail, Section F (η = 0.2)**

(h) **Port Tail, Section H (η = -0.5)**

(i) **Starboard Tail, Section G (η = 0.8)**

Figure 39. Mach 0.87 Surface Pressure Coefficient Cuts (WT C_L = 0.503)

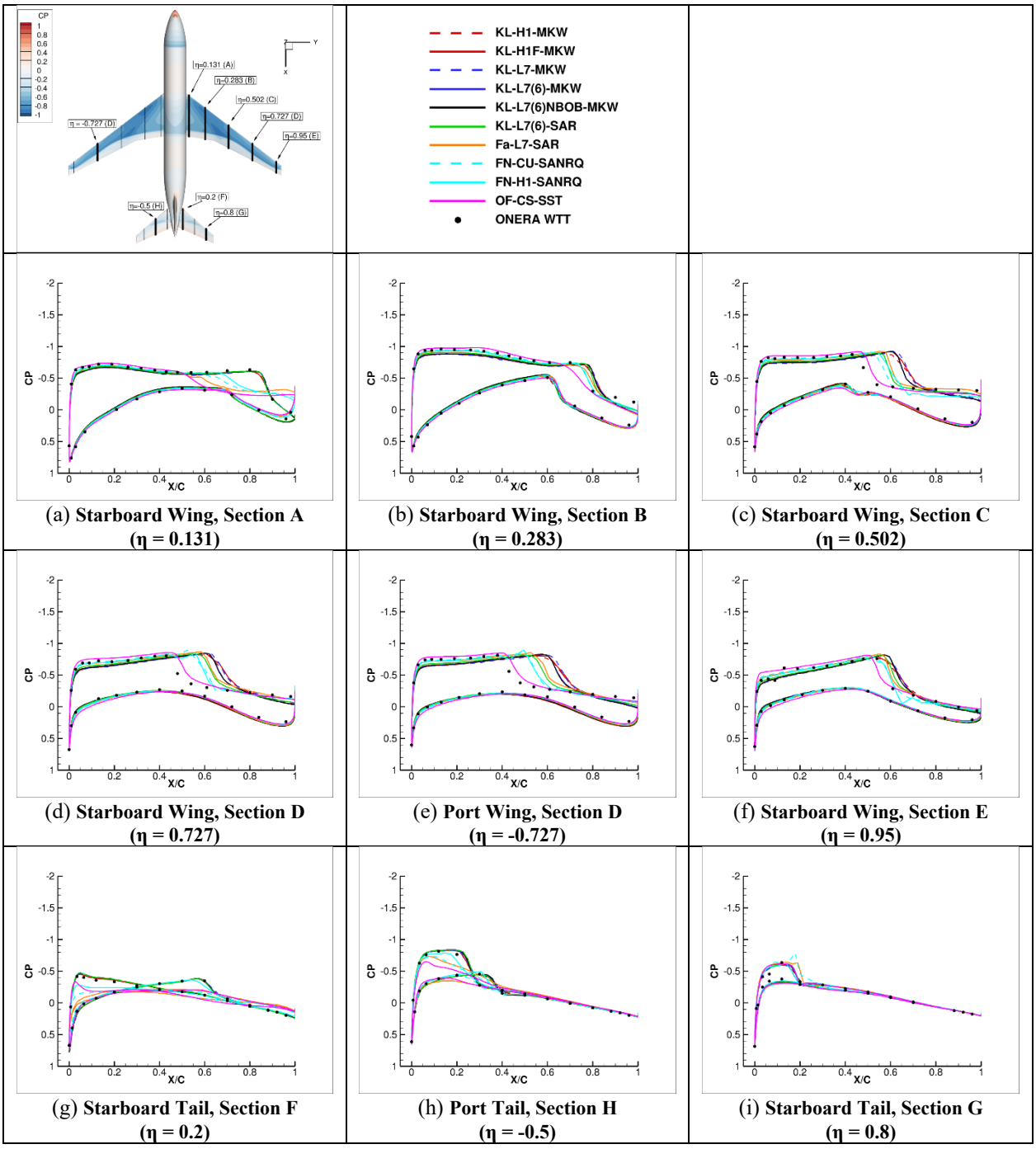

(a) **Starboard Wing, Section A (η = 0.131)**

(b) **Starboard Wing, Section B (η = 0.283)**

(c) **Starboard Wing, Section C (η = 0.502)**

(d) **Starboard Wing, Section D (η = 0.727)**

(e) **Port Wing, Section D (η = -0.727)**

(f) **Starboard Wing, Section E (η = 0.95)**

(g) **Starboard Tail, Section F (η = 0.2)**

(h) **Port Tail, Section H (η = -0.5)**

(i) **Starboard Tail, Section G (η = 0.8)**

Figure 40. Mach 0.90 Surface Pressure Coefficient Cuts (WT C_L = 0.508)

C. Case 4: Wind Tunnel Sting Increments

The objective of this case is to investigate the agreement between participant predictions of the impact of the wind tunnel support sting on the measured LRM forces and moments. These increments are one of the corrections applied to wind tunnel test data and must be estimated using methods such as CFD. All results are presented in terms of sting-on minus sting-off increments. The target lift coefficient for the static longitudinal stability increment is 0.5. The Mach number is 0.83.

Figure 41 shows the angle of attack and component lift coefficient increments due to the sting. To maintain the target total lift coefficients (0.48 and 0.52), the results show a median increase of 0.01 degree increase in angle of attack with a spread of about 0.04 degrees (excluding the OF-CS-SAR outlier). The increased angle of attack serves to increase the lift coefficient on the wings and fuselage to compensate for the loss of lift on the horizontal tail due to the sting. As shown in Fig. 42, six participants predicted an angle of attack increment of 0.02 to 0.022, which is four more than any other bin. Among the six, four used an unstructured grid with the Spalart-Allmaras turbulence model, one used an unstructured grid with the k-ω turbulence model and one used the structured overset grid with the Spalart-Allmaras model.

The drag coefficient increment agreement is pretty good as illustrated in Fig. 43. One participant predicted a 10-count increment using the structured overset grids with FUN3D, but reported they had little experience using the type of grid system with FUN3D (the motivation for the run was to have structured overset grid results from a code besides Overflow). With that result removed, the total drag coefficient clustering is good. This is confirmed in Fig. 44 which shows that eleven participants predicted a drag increment between 5.8 and 6.4 counts, a result of a 16-count increase in drag on the fuselage and a 4-count and 6-count drag decrease on the wings and tail, respectively, as shown in Fig. 43.

Figures 45 and 46 show the pitching moment coefficient increments and histograms of the pitching moment coefficient slopes at a lift coefficient of 0.5, respectively. There is considerable scatter in the total increments because of the scatter in the fuselage and tail predictions, which is reasonable since the LRM model mounts to the sting at the back end of the fuselage. The histogram shows that the bin with the most results is -4.5 to -4.0% of the sting off slope, which has four. Unfortunately, there are only three results that come in less than this range and seven that come in above it. This is consistent with an overall workshop result that pitching moment coefficient continues to be a difficult quantity to predict.

D. Case 6: β Sweep

Case 6 requires attendees to run the medium grids at transonic cruise condition (Mach=0.83, C_L=0.50) for various beta angles (0, 1, 3 and 5 degree). A total of thirteen sets of CFD results from five codes (BCFD, DLR TAU, FaSTAR, FUN3D, Kestrel and OVERFLOW), using either structured or unstructured grids with various options of turbulence model, were received. The naming convention for different code, grid system and turbulence model used in the following discussions is shown in Fig. 17.

CFD predicted results are in good agreement for vehicle lift coefficient across different codes/grids/turbulence models as shown in Fig. 47. All codes predict a consistent trend of decreasing lift coefficient for the port side and increasing lift coefficient for the starboard side of the wing as beta increases. It is interesting to point out that, within the current beta range, a relatively large C_L deviation (ΔC_L~0.01) was observed from the tail between different codes, while the total lift is very similar for all cases. It will be worthwhile to investigate the tail system grid, as well as the grid quality for the wing wake in the future workshops.

Figure 48 shows that, unlike C_L, the CFD-predicted total vehicle drag coefficients show quite a large variation between different codes for the sideslip sweep. The differences are demonstrated in absolute drag coefficient level as well as the trend of the drag coefficient change due to the sideslip angle. FN-CS-SAN shows the biggest deviation from all others across the entire sweep. The predicted drag coefficient is seen to be higher for all parts of the vehicle with the fuselage being the biggest contributor. All codes predict decreasing drag coefficient for the port (downwind) side and increasing drag coefficient for the starboard (upwind) side of the wing when beta increases. The drag coefficient variations between all codes for both wings are within a relative tight range (~10 counts).

Total and component side force coefficients predicted by all codes are in very good agreement, as seen in Fig. 49. In general, the total side force coefficient becomes more negative when beta increases, the fuselage and the tail are the main contributors while side force coefficients from both wings cancelled out for the sideslip angle range considered in this workshop.

Pitching moment coefficient predictions are compared in Fig. 50. Consistent with other test case results, there is significant variation in the vehicle pitching moment coefficient. The fuselage (except for one contribution) and wing predictions show reasonably good agreement while there is a significant amount of scatter in the tail contribution.

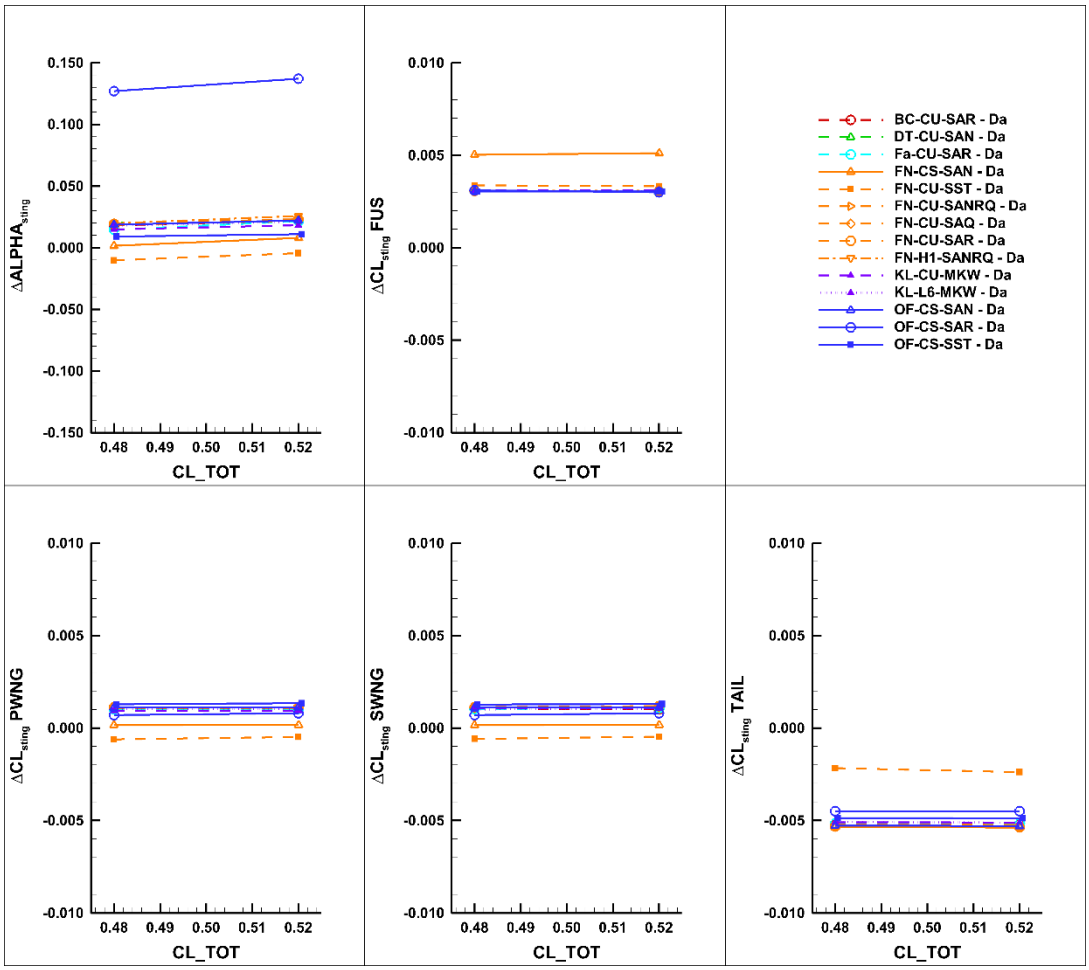

Figure 41. Increments in angle of attack and component lift coefficients due to the sting to maintain the x-axis total lift coefficients. Mach 0.83.

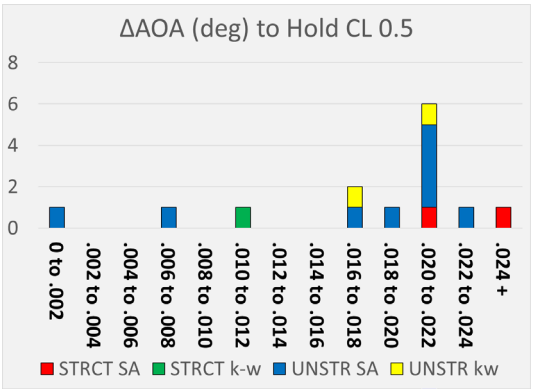

Figure 42. Histogram of the angle-of-attack increments to hold a lift coefficient of 0.5 due to the sting. Mach 0.83. The y-axis is the number of participant predictions for each drag coefficient increment range given on the x-axis.

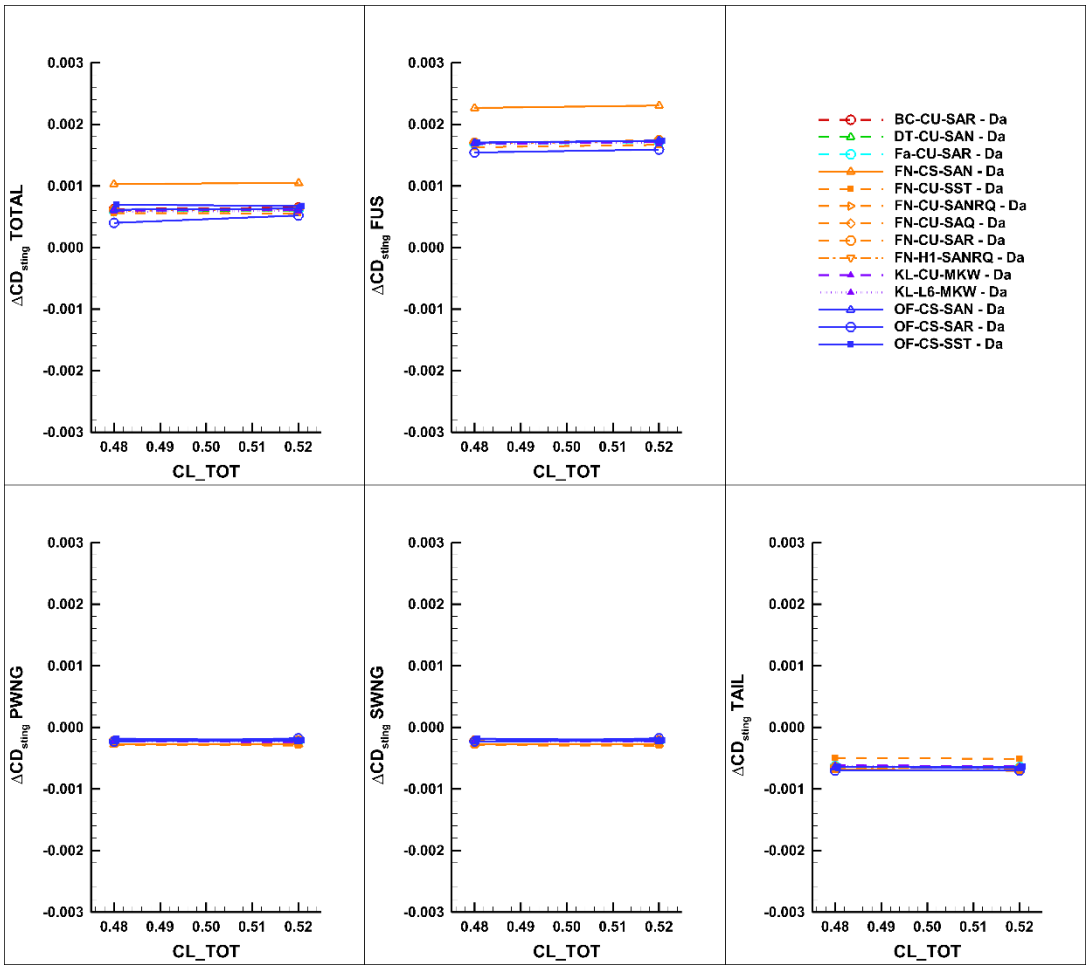

Figure 43. Increments in total and component drag coefficients due to the sting to maintain the x-axis total lift coefficients. Mach 0.83.

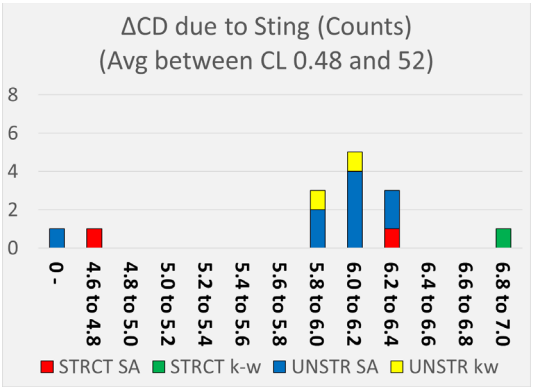

Figure 44. Histogram of the drag increment (counts) due to the sting. Mach 0.83. The y-axis is the number of participant predictions for each drag coefficient increment range given on the x-axis.

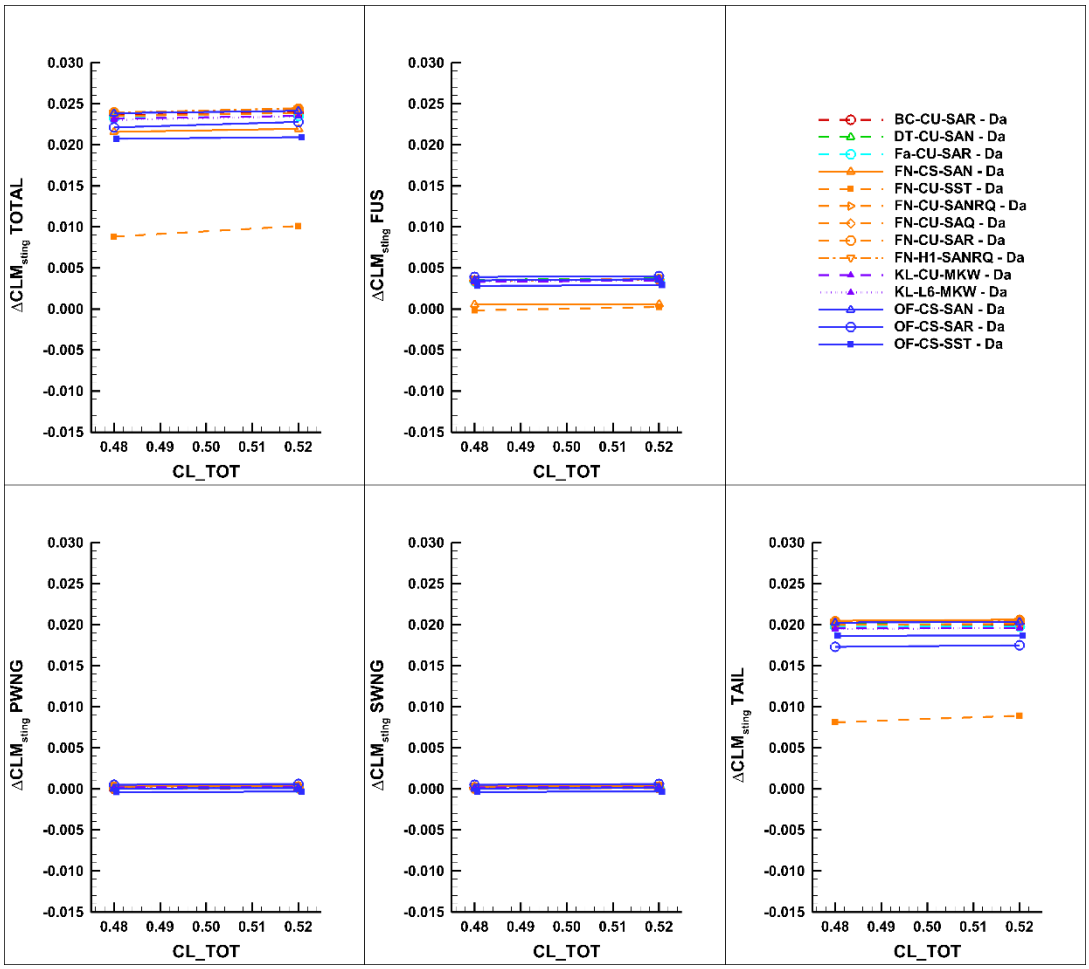

Figure 45. Increments in total and component pitching moment coefficients due to the sting to maintain the x-axis total lift coefficients. Mach 0.83.

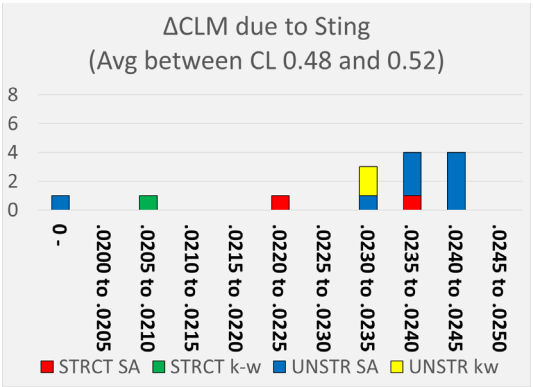

Figure 46. Histogram of the pitching moment coefficient increment due to the sting. Mach 0.83. The y-axis is the number of participant predictions for each pitching moment coefficient increment range given on the x-axis.

The rolling moment coefficient (Fig. 51) and yawing moment coefficient (Fig. 52) predictions collapse well relative to the pitching moment coefficient. This is particularly true at lower sideslip angles. A slight spread in the rolling moment coefficient predictions develops at the higher betas while a more pronounced spread develops in the yawing moment coefficient predictions, where the OVERFLOW results show a slight slope decrease and the other results show a slight slope increase.

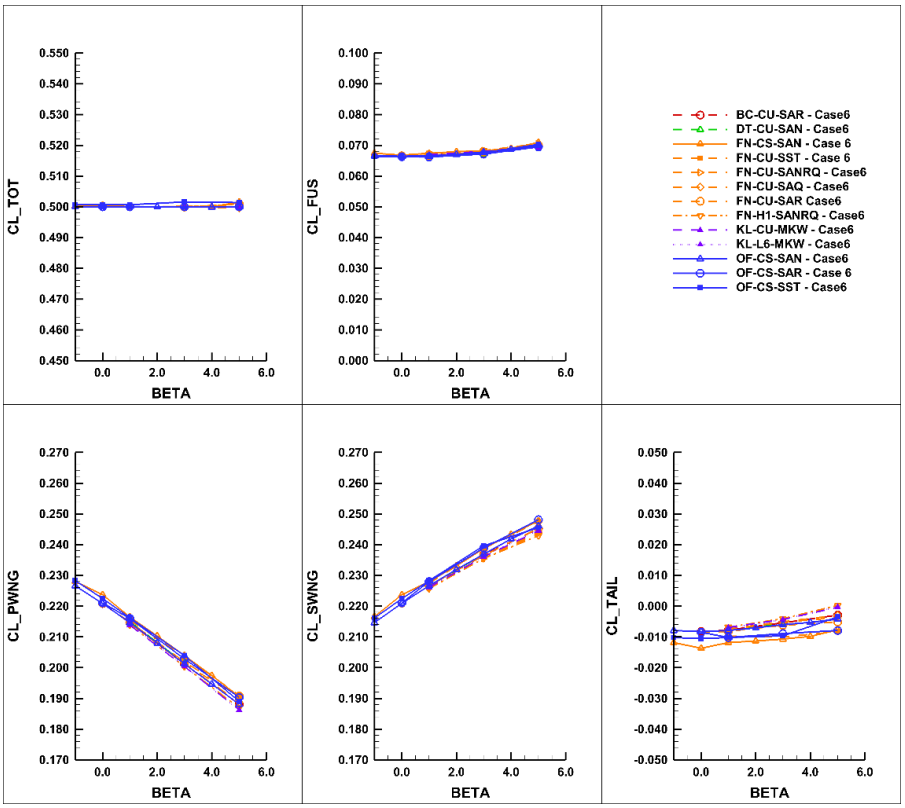

Figure 47. Lift force coefficient variation with sideslip angle. Mach 0.83, C_{Ltot}=0.5.

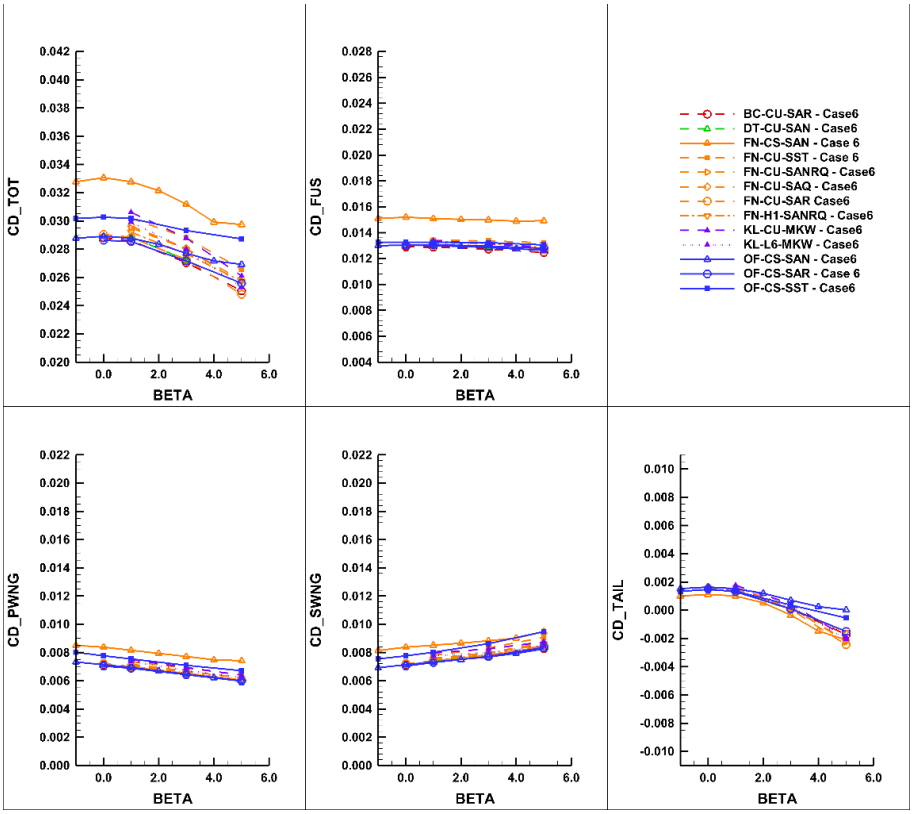

Figure 48. Drag force coefficient variation with sideslip angle. Mach 0.83, C_{Ltot}=0.5.

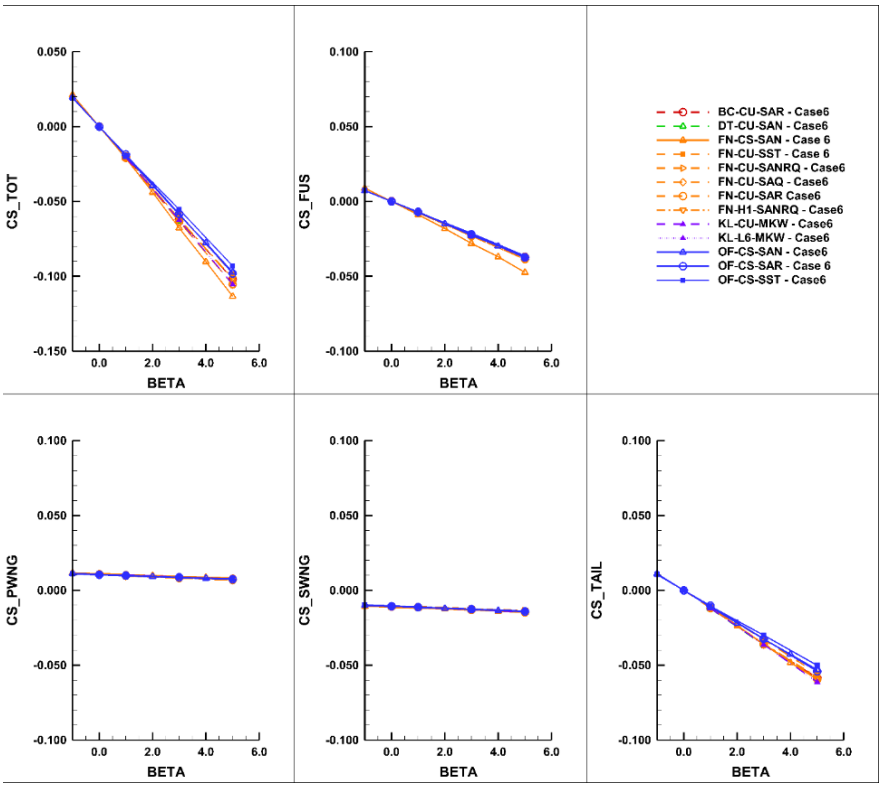

Figure 49. Side force coefficient variation with sideslip angle. Mach 0.83, C_{Ltot}=0.5.

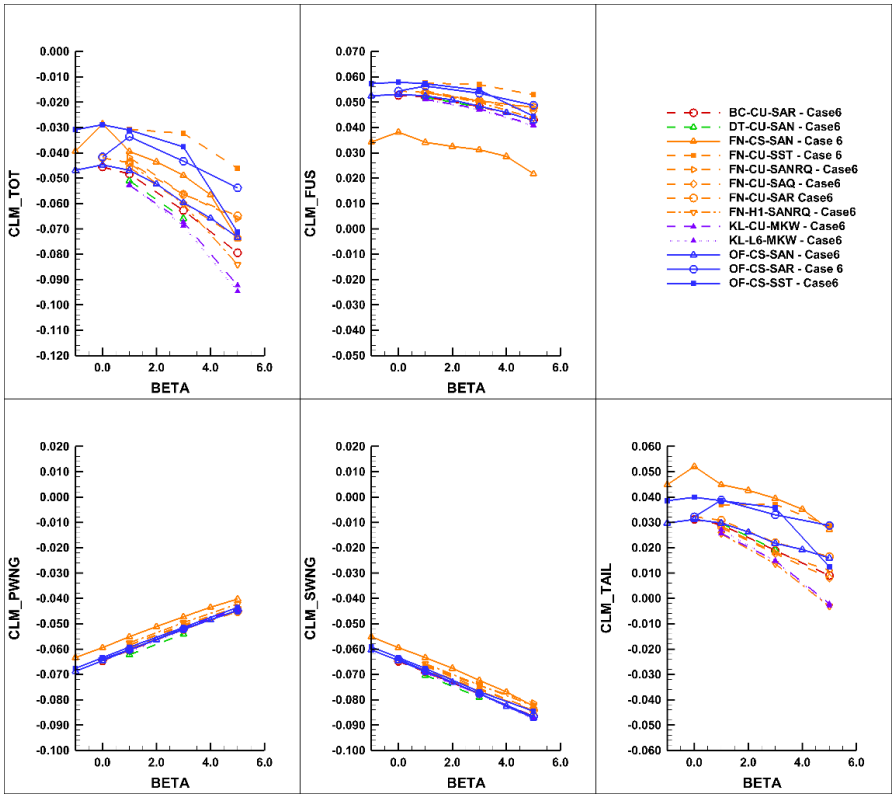

Figure 50. Pitching moment coefficient variation with sideslip angle. Mach 0.83, C_{Ltot}=0.5.

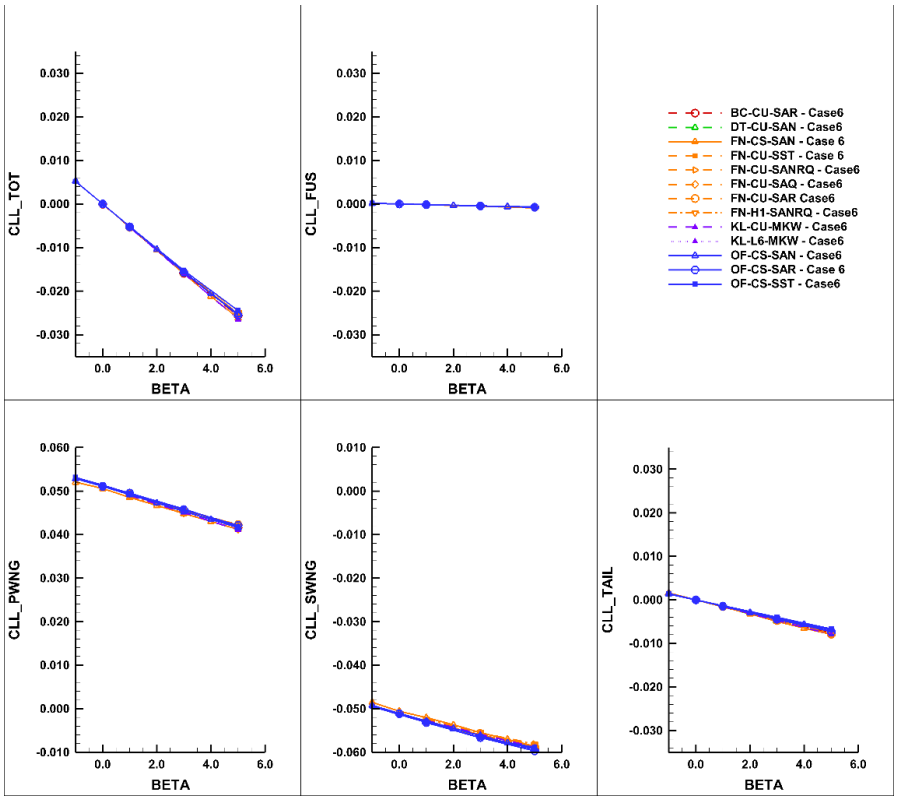

Figure 51. Rolling moment coefficient variation with sideslip angle. Mach 0.83, C_{Ltot}=0.5.

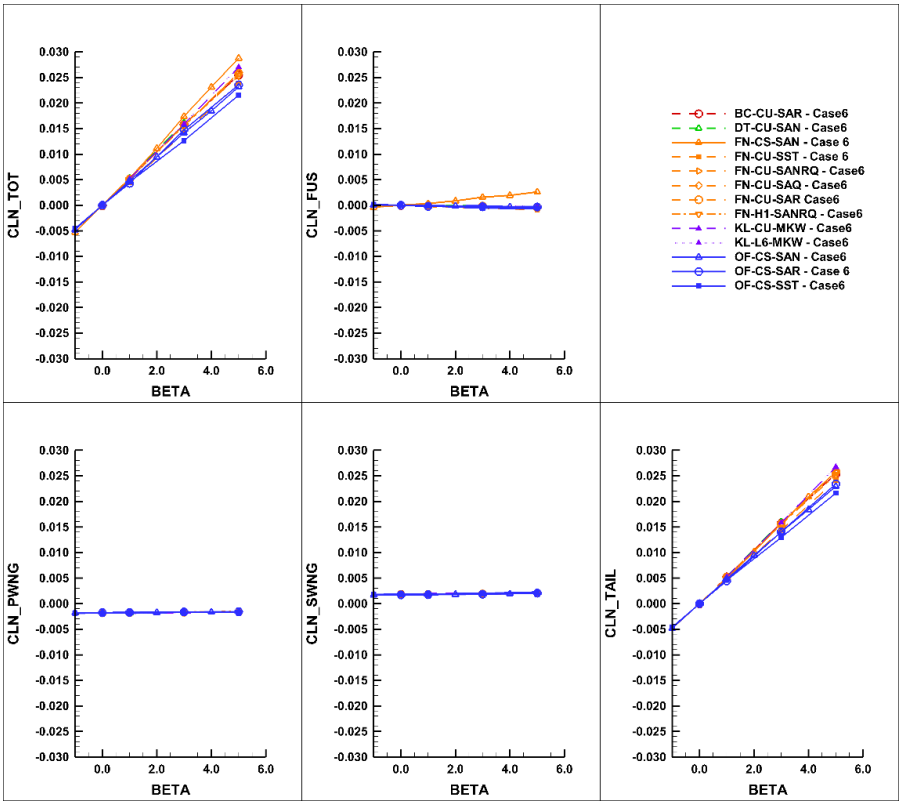

Figure 52. Yawing moment coefficient variation with sideslip angle. Mach 0.83, C_{Ltot}=0.5.

VIII. Summary and Conclusions

Results from the First AIAA Stability and Control Prediction Workshop are reported in this paper. A variant of the generic civil transport Common Research Model developed by ONERA was used as the geometry. The model consists of a fuselage, aerodynamically loaded wings, a horizontal tail and a newly developed vertical tail. It was tested in the ONERA S1MA transonic wind tunnel, where previously unpublished data at small sideslip angles were collected. The primary objective of the workshop was to assess the communities' ability to predict lateral-directional stability derivatives at transonic conditions in a blind test. A test case was also included to compare predictions of wind tunnel sting increments on drag and pitching moment.

A series of structured and unstructured grids were provided to the participants. The series span a coarse to fine resolution range permitting grid convergence data to be collected. Three participants also generated their own grids to address issues found in the provided grids. These were distributed to all participants, who had an opportunity to revisit the Mach sweep test case. Six different codes were used to generate the results, all but one formulated for unstructured grids. The Spalart-Allmaras, Menter k-ω, and k-ω SST turbulence models with a few combinations of variations were represented.

Reasonable grid convergence was achieved by most participants for all force and moment coefficients except the pitching moment coefficient. The spread in grid-converged drag coefficient is approximately 10 counts. Excluding some outliers associated with grid issues, the side force coefficient converged very well, though the converged value is about -0.0205 while the experimental value is -0.0215. The scatter in the grid-converged rolling moment coefficient is about 8% of the experimental value with a slight bias toward underprediction. In contrast, there is very little scatter (once the outliers are removed) in the converged yawing moment coefficient and a small (< 2%) bias toward underprediction. However, the scatter in the pitching moment coefficient at the finest grid level is more significant. Considering the OVERFLOW results alone, the converged values range from -0.045 and -0.025.

The Mach sweep case shows good drag coefficient agreement between the predictions (relative to the drag rise due to compressibility), however all participants underpredicted the drag coefficient at Mach 0.9. The scatter is somewhat evenly distributed across all components of the geometry. There is more scatter in the side-force coefficient predictions, due primarily to the fuselage and tail. This force is also slightly underpredicted at the Mach numbers where scatter is small. Very little consensus is achieved for the pitching moment coefficient variation. Most results overpredict the magnitude and some show a break in the wrong direction as the Mach number increases. Except for a few outliers, the rolling moment and yawing moment coefficient predictions have little scatter and follow the experimental data variation with Mach number very well.

For the wind tunnel sting increment test case (4), most predictions are in the 5.8 to 6.4-count range for drag coefficient and pitching moment coefficient increment range of 0.023 to 0.0245 for the specified flow conditions. Finally, reasonably good agreement in drag, side, yawing moment and rolling moment coefficient variations for the sideslip sweep case were achieved (with the exception of a few understood outliers).

Unfortunately, explanations behind the scatter in CFD predictions are not in reach with the data collected from the workshop participants. For instance, it remains unclear if the scatter in the pitching moment predictions is due to shock location or insufficient tail flow resolution. Additional data, such as more port wing pressure coefficient profiles and vertical tail pressure coefficient profiles, would likely shed some light on the sources of the scatter. However, it isn't clear that this will lead to best practice changes resulting in better agreement between the participants. One of the issues resulting in the scatter for the Mach sweep case may be the use of the medium grids. The use of grid adaption methods to improve shock and wing wake resolution with varying flight conditions will likely improve prediction consensus. Yet, conclusions on the source of any remaining scatter may still be intractable given the potential role of 3D component interactions. For this reason, the workshop organizers are developing a 2D case consisting of a slice of the LRM that passes through the midspan of the horizontal tail. This facilitates comparisons of grid converged forces and moments for a range of Mach numbers and lift coefficients eliminating for the moment more complex 3D effects.

Finally, there is the question of the interpretation of the results presented in this paper by S&C engineers. Do they instill confidence in CFD? Is the scatter or disagreement with wind tunnel test data (in terms of intercepts and slopes) too much to render them useless or are they sufficiently small relative to scales on the order of envelope ranges to be used in decision making or modeling? As opposed to vehicle performance, where, for example, it's important to predict drag increments due to outer mold line (OML) changes within counts, the precision required for S&C analysis can be more relaxed. Having no S&C subject matter experts as authors, we consulted some of the colleagues we have supported with CFD analysis in the past who are veteran practitioners. Their response to the prediction of the force and moment coefficient variation with Mach number at a small sideslip angle and cruise lift coefficient (Fig. 29) was reasonably positive. While there is too much disagreement in the pitching moment coefficient predictions to allow

them to be considered to set the tail incidence, the other force and moment coefficient predictions in the low-Mach range may contribute to OML decisions or be useful in flight simulations.

Acknowledgments

In addition to the authors, results presented by William Forrest, Atsushi Hashimoto, Elmer Tse, Ruben Seidler, Steve Klausmeyer, Collin Strassburger, Adam Jirasek, and Mehdi Ghoreshi at the workshop were also included in this paper. Original and revised grids were developed by Scott Sherer, Bruce Rosen, Carolyn Woeber, Kristen Shoemake, Andrew Lofthouse and Michael Bozeman.

References

[1]Hall, R.M. et al, "Computational Methods for Stability and Control (COMSAC): The Time Has Come," AIAA Paper 2005-6121, August 2005. https://doi.org/10.2514/6.2005-6121
[2]Mialon, B. et al, "European Benchmark on Numerical Prediction of Stability and Control Derivatives, " AIAA Paper 2009-4116, June 2009. https://doi.org/10.2514/6.2009-4116.
[3]Cummings, R.M., and Schutte, A., "The NATO STO Task Group AVT-201 on 'Extended Assessment of Stability and Control Prediction Methods for NATO Air Vehicles'," AIAA Paper 2014-2000, June 2000. https://doi.org/10.2514/6.2014-2000
[4]Chyczewski, T. et al, "A Position on Current Stability and Control Prediction Capabilities and a Path Forward," AIAA Paper 2020-2678, June 2020. https://doi.org/10.2514/6.2020-2678
[5]Lampton, A., and Valasek, J., "Prediction of Icing Effects on the Lateral/Directional Stability and Control of Light Airplanes," AIAA Paper 2006-6834, August 2006. https://doi.org/10.2514/6.2006-6834.
[6]Butler, J.D., "Accurate Modeling of Stability and Control Properties for Fighter Aircraft from CFD," MS Thesis, Air Force Institute of Technology, Wright-Patterson Air Force Base, Ohio, 2012.
[7]Clifton, J.D., Ratcliff, C.J., Bodkin, D.J., and Dean, J.P., "Determining the Stability and Control Characteristics of High-Performance Maneuvering Aircraft using High-Resolution CFD Simulation with and without Moving Control Surfaces," AIAA 2012-4656, AIAA Atmospheric Flight Mechanics Conference, Minneapolis MN, 2012.
[8]Frink, N.T., "Stability and Control CFD Investigations of a Generic 53-deg Swept UCAV Configuration," AIAA 2014-2133, 32nd AIAA Applied Aerodynamics Conference, AIAA AVIATION Forum, Atlanta GA, 2014.
[9]Llorca, I.B., "CFD Analysis and Assessment of the Stability and Control of a Supersonic Business Jet," M.S., Royal Institute of Technology, Stockholm, Sweden, 2015.
[10]Obara, C. J., and Lamar, J. E., "Overview of the Cranked-Arrow Wing Aerodynamics Project International," Journal of Aircraft,Vol. 46, No. 2, 2009, pp. 355–368.
[11]Cummings, R.M., and Schutte, A., "An Integrated Computational/Experimental Approach to UCAV Stability & Control Estimation: Overview of NATO RTO AVT-161," AIAA Paper 2010-4392, June 2010. https://doi.org/10.2514/6.2010-4392
[12]Cummings, R.M., "Introduction to Special Section-Computational and Experimental Aerodynamics and Stability & Control for an Agile UAV," *Journal of Aircraft*, Vol. 55, No. 2, March-April 2018, p. 453
[13]Levy, D.W. et al, "Data Summary from the First AIAA Computational Fluid Dynamics Drag Prediction Workshop," *Journal of Aircraft*, Vol. 40, No. 5, September-October 2003, pp. 875-882.
[14]Laflin, K.R. et al, "Data Summary from Second AIAA Computational Fluid Dynamics Drag Prediction Workshop," *Journal of Aircraft*, Vol. 42, No. 5, September-October 2005, pp. 1165-1178.
[15]Vassberg, J.C. et al, "Abridged Summary of the Third AIAA Computational Fluid Dynamics Drag Prediction Workshop," *Journal of Aircraft*, Vol. 45, No. 3, May-June 2008, pp. 781-798.
[16]Vassberg, J.C. et al, "Summary of the Fourth AIAA Computational Fluid Dynamics Drag Prediction Workshop," *Journal of Aircraft*, Vol. 51, No. 4, July-August 2014, pp. 1070-1089.
[17]Levy, D.W. et al, "Summary of Data from the Fifth Computational Fluid Dynamics Drag Prediction Workshop," *Journal of Aircraft*, Vol. 51, No. 4, July-August 2014.
[18]Tinoco, E.N. et al, "Summary Data from the Sixth AIAA CFD Drag Prediction Workshop: CRM Cases," *Journal of Aircraft*, Vol. 55, No. 4, July-August 2018, pp. 1352-1379.
[19]Rumsey, C.L., Slotnick, J.P., Long, M., Stuever, R.A., and Wayman, T.R., "Summary of the First AIAA CFD High-Lift Prediction Workshop," *Journal of Aircraft*, Vol. 48, No. 6, November-December 2011, pp. 2068-2079.
[20]Rumsey, C.L., and Slotnick, J.P., "Overview and Summary of the Second AIAA High-Lift Prediction Workshop," *Journal of Aircraft*, Vol. 52, No. 4, July-August 2015, pp. 1006-1025.

[21]Rumsey, C.L., Slotnick, J.P., and Sclafani, A.J., "Overview and Summary of the Third AIAA High Lift Prediction Workshop," *Journal of Aircraft*, Vol. 56, No. 2, March-April 2019, pp. 621-644
[22]Park, M.A., and Morgenstern, J.M., "Summary and Statistical Analysis of the First AIAA Sonic Boom Prediction Workshop," *Journal of Aircraft*, Vol. 53, No. 2, March-April 2016, pp. 578-598.
[23]Park, M.A., and Nemec, M., "Nearfield Summary and Statistical Analysis of the Second AIAA Sonic Boom Prediction Workshop, " *Journal of Aircraft,* Vol. 56, No. 3, May-June 2019, pp. 851-875.
[24]Rallabhandi, S.K., and Loubeau, A., "Summary of Propagation Cases of the Second AIAA Sonic Boom Prediction Workshop," *Journal of Aircraft*, Vol. 56, No. 3, May-June 2019, pp. 876-895.
[25]Rallbhandi, S.K. and Loubeau, A., "Summary of Propagation Cases of the Third AIAA Sonic Boom Prediction Workshop," AIAA Paper 2021-0229, January 2021. https://doi.org/10.2514/6.2021-0229.
[26]Park, M.A., and Carter, M.B., "Nearfield Summary and Analysis of the Third AIAA Sonic Boom Prediction Workshop C608 Low Boom Demonstrator," AIAA Paper 2021-0345, January 2021. https://doi.org/10.2514/6.2021-0345.
[27]Cartieri, A., Hue, D., Chanzy, Q., and Atinault, O., "Experimental Investigations on Common Research Model at ONERA-S1MA-Drag Prediction Workshop Numerical Results," *Journal of Aircraft*, Vol. 55, No. 4, July-August 2018, pp. 1491-1508
[28]Vassberg, J.C., DeHaan, M.A., Rivers, S.M., and Wahls, R.A., "Development of a Common Research Model for Applied CFD Validation Studies," AIAA Paper 2008-6919, August 2008. https://doi.org/10.2514/6.2008-6919.
[29]NASA Langley Research Center, "Common Research Model," http://commonresearchmodel.larc.nasa.gov/.
[30]Hue, D., et al., "Validation of a near-body and off-body grid partitioning methodology for aircraft aerodynamic performance prediction," *Computers & Fluids*, Vol. 117, 2015, pp. 196-211.
[31]Le Sant, Y., Mignosi, A., Touron, G., Deléglise, B., Bourguignon, G., "Model Deformation Measurement (MDM) at ONERA", AIAA Paper 2007-3817, June 2007. https://doi.org/10.2514/6.2007-3817.
[32]Vaucheret X., "Recent Calculation Progress on Wall Interferences in Industrial Wind Tunnels", La Recherche Aérospatiale, No. 3, pp 45-47,1988.
[33]Pistolesi, E., "Collected lectures of the principal meeting of the Lilienthal society", Considering respecting the mutual influence of system of airfoils, Berlin, 1937.
[34]Cartieri, A., and Mouton, S., "Using CFD to calculate support interference effects," AIAA Paper 2012-2864, June 2012. https://doi.org/10.2514/6.2012-2864
[35]Cartieri, A."Experimental Investigations on Common Research Model at ONERA-S2MA", AIAA Paper 2020-0779, Jan 2020. https://doi.org/10.2514/6.2020-0779
[36]NASA Langley Research Center Turbulence Modeling Resource, https://turbmodels.larc.nasa.gov
[37]Coder, J.G., Hue, D., Kenway, G., Pulliam, T.H., and Sclafani, A.J., "Contributions to the 6th AIAA CFD Drag Prediction Workshop Using Structured, Overset Grid Methods," January 2017, AIAA Paper 2017-0960. https://doi.org/10.2514/6.2017-0960
[38]Chan, W.M. et al, "Chimera Grid Tools User's Manual, Version 2.1," Moffett Field, CA, 2010.
[39]Pointwise, Software Package, Ver. 18.4R1, Cadence Design Systems, San Jose, CA, 2021
[40]HeldenMesh, Software Package, Ver. 2.09, Helden Aerospace, Acworth, GA, 2019
[41]Biedron, R.T. et al, "FUN3D Manual: 13.0," NASA TM-2016-219330, Langley Research Center, Aug. 2016
[42]Morton, S. and McDaniel, D., "A Fixed-Wing Aircraft Simulation Tool for Improving DoD Acquisition Efficiency," *Computing in Science and Engineering*, Vol. 18, No. 1, January/February 2016
[43]NASA OVERFLOW CFD code website, http://overflow.larc.nasa.gov.
[44]Cary, A.W., Dorgan, A.J., and Mani, M., "Towards Accurate Flow Predictions Using Unstructured Meshes," AIAA Paper 2009-3650, June 2009. https://doi.org/10.2514/6.2009-3650
[45]Stuermer, A., "Assessing Turbofan Modeling Approaches in the DLR TAU-Code for Aircraft Aerodynamics Investigations," AIAA Paper 2019-0277, January 2019. https://doi.org/10.2514/6.2019-0277
[46]Ishida, T., Ishiko, K., Hashimoto, A., Aoyama, T., and Takekawa, K., "Transonic Buffet Simulation over Supercritical Airfoil by Unsteady-FaSTAR Code," AIAA Paper 2016-1310, January 2016. https://doi.org/10.2514/6.2016-1310